2011

Characterization of the intragranular water regime within subsurface sediments: Pore volume, surface area, and mass transfer limitations

Michael B. Hay
U.S. Geological Survey

Deborah L. Stoliker
U.S. Geological Survey

James A. Davis
U.S. Geological Survey

John M. Zachara
Pacific Northwest National Laboratory, john.zachara@pnl.gov

Characterization of the intragranular water regime within subsurface sediments: Pore volume, surface area, and mass transfer limitations

Michael B. Hay,[1] Deborah L. Stoliker,[1] James A. Davis,[1,2] and John M. Zachara[3]

Received 3 December 2010; revised 20 September 2011; accepted 26 September 2011; published 29 October 2011.

[1] Although "intragranular" pore space within grain aggregates, grain fractures, and mineral surface coatings may contain a relatively small fraction of the total porosity within a porous medium, it often contains a significant fraction of the reactive surface area, and can thus strongly affect the transport of sorbing solutes. In this work, we demonstrate a batch experiment procedure using tritiated water as a high-resolution diffusive tracer to characterize the intragranular pore space. The method was tested using uranium-contaminated sediments from the vadose and capillary fringe zones beneath the former 300A process ponds at the Hanford site (Washington). Sediments were contacted with tracers in artificial groundwater, followed by a replacement of bulk solution with tracer-free groundwater and the monitoring of tracer release. From these data, intragranular pore volumes were calculated and mass transfer rates were quantified using a multirate first-order mass transfer model. Tritium-hydrogen exchange on surface hydroxyls was accounted for by conducting additional tracer experiments on sediment that was vacuum dried after reaction. The complementary ("wet" and "dry") techniques allowed for the simultaneous determination of intragranular porosity and surface area using tritium. The Hanford 300A samples exhibited intragranular pore volumes of ~1% of the solid volume and intragranular surface areas of ~20%–35% of the total surface area. Analogous experiments using bromide ion as a tracer yielded very different results, suggesting very little penetration of bromide into the intragranular porosity.

Citation: Hay, M. B., D. L. Stoliker, J. A. Davis, and J. M. Zachara (2011), Characterization of the intragranular water regime within subsurface sediments: Pore volume, surface area, and mass transfer limitations, *Water Resour. Res., 47*, W10531, doi:10.1029/2010WR010303.

1. Introduction

[2] In reactive groundwater transport models, the mass balance for a solute in the conventional mathematical treatment includes terms for advection, dispersion, and solid-phase reactions (e.g., sorption, ion exchange, and dissolution/precipitation); while in complex and heterogeneous porous media, this description often must be modified to account for mass transfer rate limitations [*Brusseau and Rao*, 1990; *Haggerty and Gorelick*, 1995]. Although such rate limitations may arise from multiple physical or chemical sources, it is often caused by the presence of low-flow or stagnant solution zones in diffusive contact with advective pore water, resulting from soil/sediment aggregation, stratification, or grain fracturing. This phenomenon is commonly included in the reactive transport model at the subgrid level by dividing the porosity into advective and nonadvective fractions, with diffusive mass transfer between mobile (advective) and immobile domains [e.g., *Brusseau and Rao*, 1990; *Haggerty and Gorelick*, 1995; *Koch and Flühler*, 1993; *Nkedi-Kizza et al.*, 1982; *Parker and Valocchi*, 1986; *Rao et al.*, 1980a, 1980b]. Such intra-aggregate/intragranular water domains occur over a variety of spatial scales down to the individual grain and may account for widely varying proportions of the total porosity in a packed column or saturated aquifer. The "immobile" domain might include intra-aggregate pore space on the centimeter scale or larger, where it can easily constitute several tens of percent of the total porosity in highly structured porous media [*Nkedi-Kizza et al.*, 1982; *van Genuchten and Wierenga*, 1977], as well as "intragranular" pore space which may account for a few percent or less of the total porosity [*Ball et al.*, 1990; *Wood et al.*, 1990]. This intragranular pore space (Figure 1) includes water present within soil/sediment grain fractures and small aggregates of grains that are cemented together. It contributes to the immobile fraction of the total porosity, as the transport of solutes occurs primarily by diffusion in response to concentration gradients between intragranular and extragranular water.

[3] Even when the intragranular volume is not large enough to substantially affect the transport of a nonreactive solute, the intragranular pore space may contain a significant fraction of the total surface area, thereby exerting a large effect on the transport of sorbing/exchanging solutes [*Ball et al.*, 1990, 1991; *Ewing et al.*, 2010; *Wood et al.*,

[1]Water Resources Division, U.S. Geological Survey, Menlo Park, California, USA.
[2]Earth Sciences Division, Lawrence Berkeley National Laboratory, Berkeley, California, USA.
[3]Pacific Northwest National Laboratory, Richland, Washington, USA.

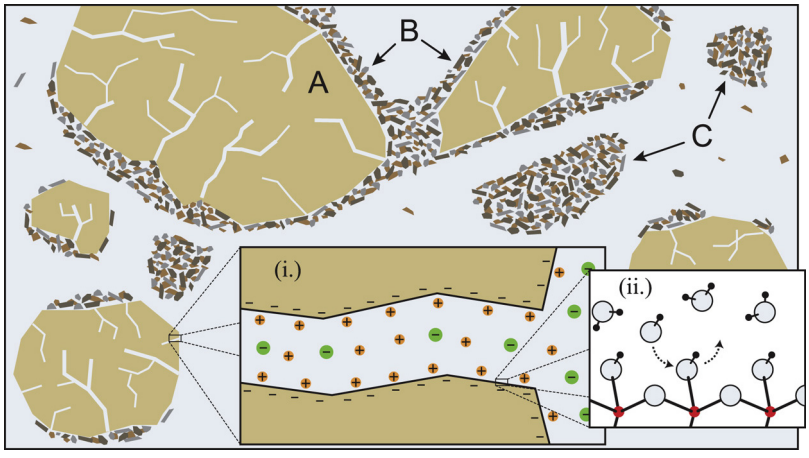

Figure 1. Grain-scale cross section of saturated aquifer sediment showing various potential contributors to "intragranular" porosity, including (A) grains with interior fractures, (B) clay coatings on fractured grains, and (C) discrete clay aggregates. (i) Magnification of an intragranular pore. Negatively charged surfaces because of clays with permanent layer charge and/or hydroxylated surfaces with PZC < solution pH are balanced by cations (orange), leading to exclusion of anions (green) within narrow pores. (ii) Hydroxylated mineral surface (e.g., metal-oxyhydroxide or clay edge), where protons may effectively adsorb via a solution-surface hydroxyl exchange.

1990]. This effect has long been recognized and studied, particularly in the context of organic contaminant transport, where models have been developed that couple sorption and physical mass transfer [*Cunningham et al.*, 1997; *Pedit and Miller*, 1994 and references therein]. Such models have varied widely in complexity and the degree to which soil/sediment intragranular properties have been explicitly included, from single-rate and distributed-rate first-order mass transfer models, where parameters are often lumped in such a way that intragranular volume is not considered explicitly [*Culver et al.*, 1997; *Deitsch et al.*, 2000], to explicit diffusion models that capture Fickian diffusion within (often assumed spherical) particles [*Ball and Roberts*, 1991; *Rügner et al.*, 1999; *Werth and Reinhard*, 1999]. Models that explicitly include sorption within intragranular domains may incorporate intragranular porosities determined independently by gas adsorption or Hg porosimetry [e.g., *Ball et al.*, 1990; *Kleineidam et al.*, 2002; *Rügner et al.*, 1999].

[4] Ingragranular diffusion/retardation can exert an equally important role in the reactive transport of inorganic contaminants. For example, the transport of adsorbing metal ions within soils or sediments may be controlled by surface complexation with reactive mineral surface functional groups that are abundant in the intragranular region. Since the exchange of solutes between the intragranular region and bulk water is limited by diffusion, the attainment of chemical equilibrium of multicomponent sorption reactions in sediments can be slow and often needs to be described by mass transfer models that are part of the reactive transport model [*Greskowiak et al.*, 2011; *Liu et al.*, 2006, 2009; *Qafoku et al.*, 2005]. Models developed to describe inorganic contaminant transport also vary in the degree to which intragranular porosity is explicitly included [e.g., *Greskowiak et al.*, 2011]. Regardless, for both organic and inorganic sorbing species, quantification of intragranular pore volumes and surface areas are potentially useful ways to constrain the mass transfer model and make them more physically meaningful.

[5] The most common methods of determining intragranular porosity and pore size distribution are mercury porosimetry and hysteresis of gas adsorption and desorption [e.g., *Ball et al.*, 1990]. In the mercury porosimetry method, elemental Hg is forced into the pore spaces under pressure, and can estimate pore volumes in the size range of 3 nm to 10 μm. Its capabilities at the lower end are limited by the high pressures required and related experimental artifacts (e.g., sample crushing). Gas adsorption/desorption can be used to determine the volumes of pores from the macropore size range (>50 nm) down to the micropore range (with the lower limit set by the diameter of the gas molecule), although its application in the meso/macropore range can be severely limited depending on the type of sorption isotherm exhibited by the substrate [*Ball et al.*, 1990; *Gregg and Sing*, 1982; *Lippens and de Boer*, 1965]. Detailed pore size distributions and pore wall surface areas can be estimated from the sorption isotherms using a variety of theoretical methods, although they typically require an assumption of an idealized pore shape (e.g., cylindrical, spherical, or slit-shaped) [*Barrett et al.*, 1951; *Gregg and Sing*, 1982].

[6] In this paper, we develop and test a batch tracer uptake and release method using tritium for estimating the total intragranular porosity and surface area. Tritium is present in the aqueous phase as tritiated water (HTO) and can exchange with labile protons at surface hydroxyl groups (Figure 1), making it a useful probe of both aqueous phase transport and surface properties. It has been extensively used as a tracer in transport studies, where it can be considered nonreactive or weakly sorbing depending on the system [e.g., *García-Gutiérrez et al.*, 2001; *Liu et al.*, 2008; *Nelson et al.*, 2003; *Nkedi-Kizza et al.*, 1982], and has also been used as a means of determining surface hydroxyl site densities on mineral surfaces [*Yates and Healy*, 1976; *Yates et al.*, 1980]. Radiotracers (including tritium) have been used previously to probe diffusion within micropores [*Smit et al.*, 1978, 1981]. Tritium diffusive transport has also been used as a means of determining

total porosity in sedimentary rock and compacted clay systems [*García-Gutiérrez et al.*, 2001; *Van Loon et al.*, 2005], where in at least one example, the authors were able to resolve different types of porosity based on diffusion rate [*Van Loon and Jakob*, 2005]. To our knowledge, however, ours is the first application of a generalized batch method for the determination of intragranular pore volume and surface area.

[7] The technique developed is demonstrated for four subsurface sediment samples collected from the Hanford, Washington 300 Area and compared with results obtained using N_2 gas adsorption. Two alternate procedures for obtaining intragranular pore volume and surface area from the tracer data are presented; one involving direct calculation from the data, and the other involving model-fitting employing a multirate mass transfer model. A spherical diffusion model is also fit to the data to further characterize the effective diffusive properties of the sediment. We also test the use of bromide (Br) as a diffusive tracer, and although preliminary results suggest that anion exclusion may be limiting bromide diffusion through the intragranular space, the technique is not sensitive enough for bromide to state this conclusively. The technique developed here represents a "diffusion-based" measure of intragranular pore volume and surface area that can complement the more traditional porosimetry techniques described above, while providing a more direct and relevant measure of the intragranular properties that influence contaminant reactive transport.

2. Materials and Methods

2.1. Sediment Description and Characterization

[8] Porosimetry analyses and batch experiments were carried out using vadose zone and seasonally saturated zone sediments collected from the Hanford 300 Area. Using an excavator, sediments were collected at multiple depths from four locations beneath the former North and South Process Ponds (two locations at each pond), sieved to <2 mm, and air-dried [*Zachara et al.*, 2005]. For the present study, we used one sample from the second North Process Pond pit (denoted NPP 2–4), one sample from the first South Process Pond pit (SPP 1–18), and two samples from the second South Process Pond pit (SPP 2–16 and 2–18, where the number after the dash indicates the depth below ground surface at the time of sampling). Sample NPP 2–4 was collected within the vadose zone, whereas SPP 1–18, 2–16, and 2–18 were collected from the region of seasonal water saturation directly above the continually saturated zone. These sediments have been characterized in a number of previous studies [e.g., *Bond et al.*, 2008; *Singer et al.*, 2009; *Stubbs et al.*, 2009; *Zachara et al.*, 2005].

[9] Surface area and porosity were determined by N_2 gas adsorption after 72 h of drying at 105°C (Micromeritics Tristar 3000). Full adsorption-desorption isotherms were collected at liquid-nitrogen temperature within a relative pressure range of 0.05–0.998, from which Brunauer, Emmett, and Teller (BET) surface areas, *t*-plots, and pore-size distributions were generated. The BET *c* parameter for all samples fell within a range of 177–238, which is an acceptable range for application of the BET equation [*Davis and Kent*, 1990; *Gregg and Sing*, 1982]. The *t*-plot, which plots the quantity of gas adsorbed as a function of the calculated film thickness, can be used to determine exposed surface area and filled-pore volumes on the basis of curve fits to the linear portions of the plot [*Leofanti et al.*, 1998; *Lippens and de Boer*, 1965 and references therein]. The statistical film thickness was calculated using the Harkins-Jura equation:

$$l_{film}\ [\mathrm{nm}] = \left(\frac{13.99}{0.034 - \log(p/p^0)}\right)^{1/2}. \quad (1)$$

[10] Additional N_2 gas sorption isotherms were collected on SPP 1–18 using an instrument capable of reaching relative pressures below 1×10^{-6} (Quantachrome Autosorb-1-MP). For comparison with the *t*-plot method, the adsorption isotherms were analyzed using the Horváth-Kawazoe and Saito-Foley methods to obtain pore size distributions.

2.2. Batch Experiments With Tritiated Water and Bromide

[11] The batch experiments involved pre-equilibration of sediment with an artificial groundwater (AGW 4, pH 8.65, ionic strength 0.0114 [*Bond et al.*, 2008]) containing either a tritiated water or bromide tracer, followed by replacement of the bulk solution by tracer-free artificial groundwater. Intragranular pore volumes and surface areas were estimated based on the total quantity of tracer released (as described in section 2.3), while mass transfer kinetics were characterized based on tracer released as a function of time (section 2.4). The surface-bound fraction of tritium was estimated using a "dry-batch" (DB) technique: (1) the sediment was pre-equilibrated with the tritiated solution, (2) the intragranular and extragranular water was removed via freeze drying, then (3) the dried sediment was resuspended in a tritium-free solution and monitored over time. The surface-bound and aqueous-phase intragranular tracer fractions were then quantified together using a "wet-batch" (WB) technique: (1) the sediment was pre-equilibrated with the tritiated solution, (2) the extragranular bulk water was removed by repeated centrifugation, decanting, and backfilling with tracer-free solution, then (3) the tracer concentration in solution was monitored over time after the final backfill with tracer-free solution. Experiments involving bromide were performed using the WB technique only. Given the experimental procedure, only the intragranular pores present within aggregates and fractured grains with the cohesive strength to endure suspension, long-term mixing, and repeated centrifugation and resuspension are probed using this technique.

[12] In the tritium WB experiments, sediment was suspended in artificial groundwater spiked with tritiated water (850 nCi mL^{-1}) in 500 mL polycarbonate centrifuge bottles at a 1500 g L^{-1} sediment-to-solution ratio. Although the same sediment-to-solution ratio was used throughout, 10 g of sediment was used in each SPP 1–18 experiment, while the SPP 2–18, SPP 2–16, and NPP 2–4 experiments were each conducted using 15 g of sediment. After suspension, the bottles were placed on an orbital shaker table to equilibrate. Samples SPP 2–18, SPP 2–16, and NPP 2–4 were pre-equilibrated for between 208 and 211 d ($\sim$7 months), while three experiments with SPP 1–18 were conducted with respective pre-equilibration times of 2, 11, and 62 d to test pre-equilibration time as a variable. After pre-equilibration, the washing steps were repeated until the aqueous concentration was diluted to $\sim$0.1% of its initial

value. The objective of this procedure was to exchange the bulk solution to the greatest extent possible while minimizing the disturbance of the intragranular pore water. The washing procedure required 3–4 centrifuge and backfill cycles, performed as rapidly as possible (within 1 h or less). Regardless of the amount of sediment present (10–15 g), all samples received 30 mL of tracer-free solution on the final backfill to provide enough solution for long-term sampling. The solution was then subsampled over 26 weeks to monitor tracer release. Tritium concentrations in the samples were measured by liquid scintillation counting (Beckman LS 6500) and were corrected for tritium decay over the course of the experiment. All experiments were conducted in duplicate. An example of the type of data collected in the tritium WB experiment is shown in Figure 2 for the SPP 1–18 62-d pre-equilibration experiment, where time $t = 0$ is taken to be the start of the tritium release stage after removal of the tritiated solution (i.e., the moment at which the last addition of tracer-free solution was added to the sediment).

[13] Tritium-hydrogen exchange on the surface was estimated for samples SPP 1–18 and SPP 2–18 using the "DB" method. Samples were pre-equilibrated with tritium-spiked AGW for 2 d (SPP 1–18) or 11 d (1–18 and 2–18) in a 400 g L^{-1} sediment-to-solution ratio in 50 mL polycarbonate Oak Ridge centrifuge tubes placed on an end-over-end rotator. After pre-equilibration, the tubes were centrifuged and the bulk water decanted. The tubes, containing sediment and residual bulk solution, were flash-frozen in liquid nitrogen and placed under vacuum in a glass manifold. After sublimation of the bulk solution within the first 24 h, the pressure in the vacuum manifold was maintained below 1 mTorr (the lower limit of the thermistor vacuum gages) using a rotary pump-backed diffusion pump and a liquid nitrogen cold trap for an additional 7 d to remove intragranular and physisorbed water. After drying, the sediment was resuspended in tracer-free AGW, and the tubes were subsampled to determine tritium content over a 6-week period.

[14] Similar WB experiments were also performed for sample SPP 1–18 using bromide ion as a tracer. Pre-equilibration, washing, and tracer monitoring ("release") stages were conducted as above using a Br amended AGW (350 ppm), with pre-equilibration times of 2 and 65 d. The bromide samples were acidified and analyzed on an Inductively Coupled Plasma Mass Spectrometer (Perkin Elmer ELAN DRC II). Although the detection limit for Br by ICP-MS is as low as 0.03 ppb [*Wang and Jiang*, 2008], the lowest calibration standard used in this work was 8 ppb. The calibration curve was linear down to this value, and the lowest sample concentration measured was >12 ppb.

2.3. Tritium-Hydrogen Surface Exchange and Intragranular Pore Volume Calculations

[15] The concentration of tritium-hydrogen exchange sites on the sediment surfaces, S (mol g^{-1}), was estimated from the tritium release data obtained in the DB experiments using the following relation:

$$q_{rel} = m\,S\,(x_i - x_f), \tag{2}$$

where q_{rel} is the total moles of tritium released into solution after drying and resuspension, x_i is the initial fraction of exchange sites occupied by tritium at time $t = 0$ (the moment at which sediment is resuspended after drying), x_f is the final tritium-occupied exchange site fraction after sorptive/diffusive equilibrium has been attained ($t > t_{eqlb}$), and m is the original (air-dried) sediment mass. The estimation of q_{rel} included the total tritium in solution at equilibrium as well as the tritium removed on each sampling. The DB data were also used to estimate the fraction of S residing in the extragranular and intragranular regions (f^{eg} and f^{ig}, respectively, where $f^{eg} = 1 - f^{ig}$), as described in the section 3.

[16] It is expected that there is no substantial equilibrium fractionation in the partitioning of hydrogen isotopes between aqueous and surface phases within experimental error (i.e., no substantial isotope preference on hydroxyl exchange) based on the earlier work using this method [*Yates and Healy*, 1976; *Yates et al.*, 1980]. Therefore, at equilibrium, x_i and x_f are assumed equal to the mole fractions of tritium in the aqueous phase at their respective

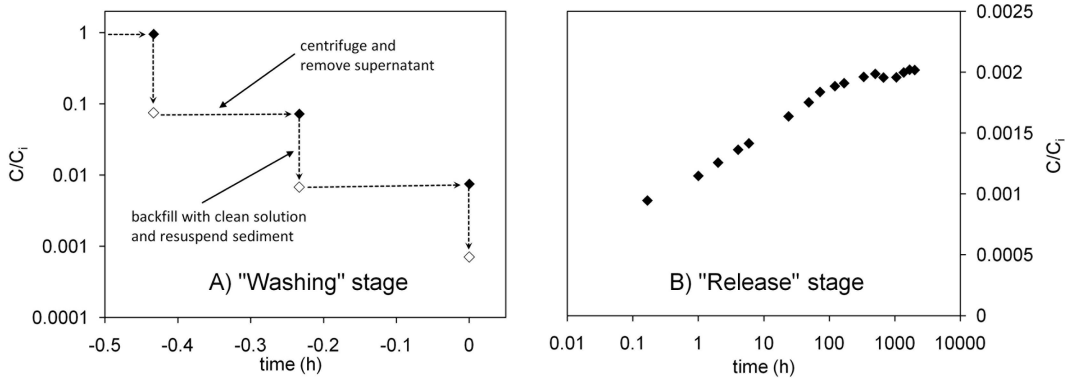

Figure 2. Tritium release in the SPP 1–18 62-d pre-equilibration WB experiment during washing and release stages (A and B, respectively). Concentrations are normalized by the initial solution concentration at the start of the wash. Solid diamonds are measured values, open diamonds are calculated values based on removed and backfilled solution volumes during the centrifugation steps in the sediment washing stage. Time $t = 0$ was assigned as the moment the final backfill volume was added to the sample at the end of the washing stage. Placement of the open diamonds on the time axis assumes that sediment resuspension occurs rapidly after each addition of tracer-free solution.

time points. The initial concentration corresponds to the last measured solution concentration before flash-freezing and vacuum drying, and the final concentration corresponds to the average aqueous concentration after time t_{eqlb}.

[17] For convenience in calculations, S (with units of mol g^{-1}) was converted to an exchange coefficient K_E (L kg^{-1}), defined by the equation

$$Q_{surf} = K_E C, \tag{3}$$

where $Q_{surf} = q_{surf}/m$ is the concentration of adsorbed solute on a sediment mass basis (mol g^{-1}) and C is the aqueous solute concentration for a solution in equilibrium with the surface. Because the hydrogen isotopes are expected to exchange nonpreferentially within experimental uncertainty, K_E applies equally to hydrogen and tritium. Therefore, for $Q_{surf} = S$, C is the total solution hydrogen concentration (110.8 moles L^{-1}; i.e., two times the molarity of water).

[18] Intragranular pore volumes, v^{ig}, were calculated from the tritium release in the WB experiments in a similar manner. The tritium released into tracer-free bulk solution, q_{rel}, includes contributions from surface and aqueous phases in the intragranular region, balanced by readsorption in the extragranular region, which gives the following mass balance expression:

$$q_{rel} = -\Delta q^{ig}_{aq} - \Delta q^{eg}_{surf} - \Delta q^{ig}_{surf} \tag{4}$$

with $\Delta q^{ig}_{aq} = v^{ig}\Delta C^{ig}_{aq}$ (see Appendix A for further details). For reasons described in the appendix, we only consider the tritiated water released during the release stage in calculating the intragranular pore volume; specifically, the tracer released between $t = 0$ (see Figure 2A) and $t > t_{eqlb}$. This required specifying an initial $t = 0$ intragranular tritium concentration. To proceed, we assume here that tritiated water release from the intragranular region is negligible during the washing stage, such that the intragranular concentration at $t = 0$ is still the same as it was on pre-equilibration ($C^{ig}_{t=0} = C_i$). The validity of this assumption and attempts to explicitly include the washing stage data in the estimation of intragranular pore volume are discussed in Appendices A and C.

[19] In this work, intragranular pore volume is typically expressed either on a sediment mass basis as $V^{ig} = v^{ig}/m$ (mm^3 g^{-1}), or on a sediment volume basis as $\varepsilon = \rho V^{ig}$ (a unitless fraction or percentage), where ρ is the sediment "skeletal" (or "true") density, assumed to be 2.8 g cm^{-3} for all four samples. A^{ig} is used to refer to the intragranular surface area (strictly, the surface area of pores that constitute V^{ig}).

2.4. Mass Transfer Modeling

[20] Tritium release data were modeled using both a multirate first-order mass transfer approach [e.g., *Haggerty and Gorelick*, 1995] and an explicit spherical diffusion model. In the multirate model, the aqueous phase is divided into a single extragranular domain representing the bulk aqueous phase and a series of intragranular water domains that collectively represent the intragranular pore space. The mass balance expression is given by

$$(\theta^{eg} + f^{eg}\rho_b K_E)\frac{\partial C^{eg}}{\partial t} + \sum_{j=1}^{n}\left[\left(\theta^{ig}_j + f^{ig}_j \rho_b K_E\right)\frac{\partial C^{ig}_j}{\partial t}\right] = 0, \tag{5}$$

where θ^{eg} is the extragranular region porosity, θ^{ig}_j is the porosity of intragranular domain j ($\sum_j \theta^{ig}_j = \theta^{ig}$), ρ_b is the bulk density of the sediment suspension, C^{eg} is the aqueous tracer concentration in the extragranular region, C^{ig}_j is the aqueous tracer concentration in intragranular domain j, f^{ig}_j is the fraction of tritium-hydrogen exchange sites in intragranular domain j ($\sum_j f^{ig}_j = f^{ig} = 1 - f^{eg}$), and n is the total number of intragranular domains. The rate of mass transfer between the extragranular domain and each intragranular domain is treated as first-order with respect to the tracer concentration gradient:

$$\frac{\partial C^{ig}_j}{\partial t} = \frac{\alpha_j}{R^{ig}_j}\left(C^{eg} - C^{ig}_j\right), \tag{6}$$

where α_j is the mass transfer rate coefficient and R^{ig}_j is the intragranular retardation coefficient, given by

$$R^{ig}_j = 1 + \frac{f^{ig}_j \rho_b K_E}{\theta^{ig}_j} = 1 + \frac{\rho_b K_E}{\theta^{ig}} = R^{ig}; \tag{7}$$

since it is assumed that tritium-hydrogen exchange sites are uniformly distributed in the intragranular region. $C^{eg}(t)$ and $C^{ig}_j(t)$ were obtained for a given set of θ^{ig}_j and α_j by numerically solving equations (5) and (6) using an implicit finite difference algorithm.

[21] The mass transfer coefficients, α_j, were assumed to be lognormally distributed across pore space. This was accomplished in the numerical model by dividing intragranular pore space into n equal volume domains, then determining α_j values using the lognormal cumulative distribution function (cdf),

$$\mathrm{cdf}(\alpha_j; \mu, \sigma) = \frac{1}{2} + \frac{1}{2}\mathrm{erf}\left[\frac{\ln(\alpha_j) - \mu}{\sigma\sqrt{2}}\right], \tag{8}$$

where μ and σ are the mean and standard deviation, respectively, describing the normal distribution of $\ln(\alpha)$. Specifically, discrete cdf(α_j) values were determined, where

$$\mathrm{cdf}(\alpha_j) = \frac{2j-1}{2n}, \quad 1 \le j \le n, \tag{9}$$

which were then used to determine α_j using equation (8). In implementing the distributed-rate model, an n value of 100 was typically used, taking care to ensure that the numerical solution was insensitive to a further increase in n.

[22] The mass balance expression for diffusion from a sphere is given by

$$(\theta^{eg} + f^{eg}\rho_b K_E)\frac{\partial C^{eg}}{\partial t} + \left(\theta^{ig} + f^{ig}\rho_b K_E\right)\frac{\partial C^{ig}}{\partial t} = 0, \tag{10}$$

with $C^{ig}(t)$ governed by Fickian diffusion [e.g., *Ball and Roberts*, 1991; *Crank*, 1975]:

$$R^{ig}\frac{\partial C^{ig}}{\partial t} = \frac{D}{a^2}\left(\frac{\partial^2 C^{ig}}{\partial R^2} + \frac{2}{R}\frac{\partial C^{ig}}{\partial R}\right), \tag{11}$$

where D is the diffusion coefficient, a is the sphere radius, and $R = r/a$, where r is the radial coordinate variable.

Equations (10) and (11) were solved numerically to determine $C^{eg}(t)$ and $C^{ig}(r,t)$ with an implicit finite difference approach, using the radial-coordinate finite difference approximations suggested by *Crank* [1975].

[23] Model inputs included sediment mass; initial solution volume, including sediment hydration water; initial aqueous concentration in extra- and intragranular regions (specified for the WB model) or total initial tracer in the system (specified for the DB model and assumed to be uniformly distributed on extra- and intragranular zone surfaces at the start); intragranular pore volume; K_E and f^{eg} values for tritium-hydrogen exchange; and either lognormal distribution parameters (μ, σ, and n) or spherical diffusion model parameters (D and a, the sphere radius). The model output was fitted to the experimental data by iterative adjustment of the input parameters and rerunning of the model using UCODE [*Poeter et al.*, 2005].

3. Results

3.1. N_2 Gas Sorption Isotherms and *t*-plot Analyses

[24] The N_2 gas adsorption/desorption results indicate a type IV isotherm with an H3-type hysteresis loop [e.g., *Leofanti et al.*, 1998; *Sing*, 1989]. The isotherm collected on sample SPP 1–18, qualitatively similar to those collected on the other three samples studied, is shown in Figure 3A. This type of isotherm is characterized by a sharp, asymptotic increase in the volume of gas adsorbed as the relative pressure approaches unity. This type of behavior is broadly recognized to correspond to capillary condensation in slit-shaped pores between flat or plate-like surfaces, and as such is very commonly observed in clay mineral aggregate systems [*Leofanti et al.*, 1998; *Sing*, 1989]. The hysteresis loop closes on the low end at $p/p^0 = 0.45$, corresponding to the critical Kelvin radius for capillary condensation. In the desorption curve, all pores with radii at or below the Kelvin radius empty simultaneously at this relative pressure. This corresponds to a pore width of ~2.4 nm for parallel sheets and a pore diameter of ~3.6 nm for cylindrical pores [*Gregg and Sing*, 1982], herein referred to as the "Kelvin cutoff." The desorption isotherm is also affected by pore network effects in which the evacuation of large, filled pores is controlled by the radius of pore openings, rather than the pore body [*Sing*, 1989 and references therein]. The desorption isotherm therefore suggests a significant quantity of pores controlled by pore necks narrower than the Kelvin cutoff (a 2.4 nm width assuming a slit-pore geometry). More quantitative descriptions of pore volume and surface area as a function of pore size were determined from the isotherms using the *t*-plot method, described below. Although the Barrett, Joyner and Halenda (BJH) method is also a very common means of extracting pore size distributions from gas adsorption isotherms, the results of this analysis are highly unreliable for type IV/H3 isotherms [*Gregg and Sing*, 1982]; these results are therefore not included here. A discussion of additional isotherm analysis methods is included in Appendix B.

[25] The *t*-plots generated using the N_2 adsorption and desorption isotherms are shown in Figure 3B for SPP 1–18. Separate linear fits were obtained for the data between 0.3 and 0.5 nm and between 0.7 and 1.2 nm. The ordinate intercept for the fit to the lower range represents the volume of pores with a width less than or equal to ~0.6 nm, or two times the lowest calculated film thickness, since the *t*-plot remains linear down to that value. Thus, all these pores fall below the "micropore" cutoff of 2 nm [*Gregg and Sing*, 1982]. The adsorption and desorption isotherms yield very similar fits in this range and indicate <0.6 nm pore volumes between 1.0 and 2.6 $mm^3\ g^{-1}$ for the Hanford samples studied (Table 1). Estimates of <0.6 nm pore surface area were obtained by subtracting the *t*-plot exposed surface area from the BET surface area for each sample; these values are in the range of 2.2–5.7 $m^2\ g^{-1}$, accounting for 14%–24% of the total surface area (Table 1). This procedure for obtaining pore surface area is somewhat questionable; at the very least, the values will have large uncertainties associated with them, given that each is a small number obtained as the difference in two larger numbers.

[26] The upper ends of the <0.6 nm pore volume and surface area ranges correspond to sample NPP 2–4, which also exhibits the highest BET surface area. This is most likely because of a difference in the texture of grain coatings on the NPP 2–4 sediment relative to the SPP sediments, resulting from a greater exposure to waste solutions from the process ponds, which alternated between highly acidic (pH 1.8) and highly basic (pH 11.4) during the

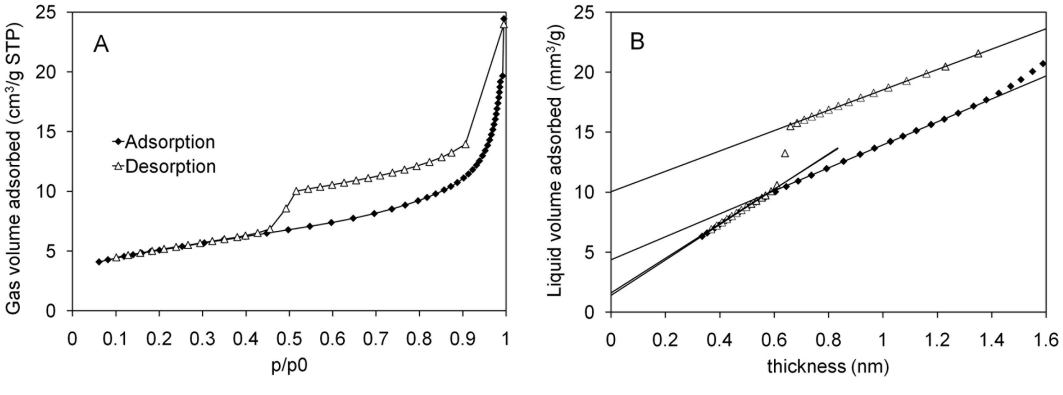

Figure 3. N_2 gas adsorption-desorption results for sample SPP 1–18. (A) Isotherms for N_2 adsorption (solid diamonds) and desorption (open triangles). (B) *t*-plot analyses, showing straight-line fits to the data from 0.3 to 0.5 nm and from 0.7 to 1.2 nm.

Table 1. BET Surface Areas and *t*-Plot Results from N_2 Gas Adsorption/Desorption[a]

	Pore Volume ($mm^3\ g^{-1}$)				Surface Area ($m^2\ g^{-1}$)				
	<0.6 nm		<Kelvin Cutoff			<0.6 nm		<Kelvin Cutoff	
Sample	Adsorption[b]	Desorption[b]	Adsorption	Desorption	BET	Adsorption	Desorption	Adsorption	Desorption
SPP 1–18	1.38	1.57	4.39	9.93	17.9	3.3 (0.18)[c]	3.5 (0.20)	8.4 (0.47)	9.2 (0.51)
SPP 2–18	1.02	1.08	3.33	9.55	15.1	2.4 (0.16)	2.2 (0.14)	6.2 (0.41)	8.1 (0.54)
SPP 2–16	1.13	1.32	3.28	9.77	16.8	2.7 (0.16)	2.7 (0.16)	6.5 (0.39)	8.3 (0.49)
NPP 2–4	2.10	2.57	5.75	11.68	24.2	4.9 (0.20)	5.7 (0.24)	11.5 (0.48)	13.3 (0.55)

[a]All measurements were performed in duplicate. Standard deviations between measurements (not shown) were <0.8% of the average for BET and between 0.01% and 6.0% (typically ~1%) of the average for all *t*-plot parameters.
[b]Adsorption quantities were derived from the adsorption curve; desorption from the desorption curve.
[c]Numbers in parentheses give quantities as the fraction of total BET surface area.

lifetime of the ponds [*Dennison et al.*, 1989]. Previous studies have demonstrated that NPP 2–4 contains higher concentrations of accumulated waste material (present in mixed Cu-U(VI) precipitates such as metatorbernite) relative to the SPP sediment [*Arai et al.*, 2007; *Bond et al.*, 2008; *Catalano et al.*, 2006; *Zachara et al.*, 2005]. Electron microscopy studies of sample NPP 2–4 revealed sediment grain coatings that appeared thicker, denser, and more finely grained than comparable uncontaminated sediments, presumably resulting from the interaction of the sediment with the waste solution [*Stubbs et al.*, 2009], and these coatings may be contributing to the higher surface areas and pore volumes observed here.

[27] At higher relative pressures, the *t*-plots are affected by capillary condensation in "mesopores," classically defined as pores with a width between 2 and 50 nm [*Gregg and Sing*, 1982]. The desorption curve exhibits a sharp step near 0.6 nm corresponding to the hysteresis loop closure at $p/p^0 = 0.45$, but appears linear between 0.7 and 1.2 nm, suggesting that film thinning rather than pore evacuation may be dominant in this range of the isotherm as gas is desorbed. This cannot be stated unambiguously, however, as it is possible that the effects of increased exposed surface area and pore evacuation balance to yield a *t*-plot that is nearly linear in this region. Regardless, the fitted line between 0.7 and 1.2 nm yields a pore volume estimate that is assumed to be valid at least at the low end of this thickness range, just before pore evacuation at the Kelvin cutoff. The results from this part of the *t*-plot are therefore interpreted as the volume and surface area of pores with pore width less than or equal to the Kelvin cutoff width (2.4–3.6 nm), in addition to wider pores controlled by pore throats of this size, thereby encompassing all of the micropore and part of the mesopore volume of the sample. The samples studied exhibited pore volumes of 9.6–11.7 $mm^3\ g^{-1}$ and surface areas of 8.1–13.3 $m^2\ g^{-1}$ (49%–55% of total) for pores that fall within this category, again with the larger values corresponding to sample NPP 2–4 (Table 1).

[28] The adsorption *t*-plots also exhibit a decrease in slope above 0.6 nm, suggesting a reduction in exposed surface area with gas adsorption, but without the sharp increase in adsorbed volume that would signify capillary condensation. The dominant mechanism here is more likely a filling of the mesopores by a gradual increase in film thickness without capillary nucleation, as one would have between parallel surfaces and double-ended pore necks. The fitted line to this portion of the adsorption isotherm yields alternate values for pore volume and surface area (Table 1). These values are less than the values obtained from the desorption isotherm, partly because of the pore-filling mechanism described above, but also because it does not include contributions from larger pores with small pore openings. Interestingly, the volumes predicted from adsorption and desorption curves differ much more strongly than the surface areas. This is also consistent with a strong contribution in the desorption isotherm from large pores with small pore openings (i.e., pores with relatively small surface area-to-volume ratios).

[29] For sample SPP 1–18, a N_2 sorption isotherm was also obtained using a lower-pressure gas adsorption instrument for comparison. To test the relative robustness of the *t*-plot analyses, the adsorption isotherm was analyzed using additional micropore size-distribution methods for comparison with *t*-plot results. These results are given in Appendix B.

3.2. Tritium Dry-Batch Results: Estimation Of Tritium-Hydrogen Exchange

[30] After resuspension of the vacuum-dried, tritium-reacted sediment in tritium-free solution, the bulk solution tritiated water concentration was monitored until a clear steady-state tracer concentration was observed. In all three experiments, ~70%–80% of the adsorbed tritium was released before collection of the first data point at 0.7 h, after which tritium release followed a strikingly log linear trend before reaching equilibrium (Figure 4). The equilibrium tracer concentration was estimated from the average of the last three data points, represented by the horizontal fitted lines in Figure 4. For comparison, a qualitative estimate of the time required to reach equilibrium for each data set, t_{eqlb}, was obtained as the crossing point between a straight line fitted to the log linear portion of the data and the equilibrium line. These results suggest that a steady-state tracer concentration was achieved after ~200 h without a strong dependence on sample source or pre-equilibration time. Interestingly, even the 2-d pre-equilibration yielded a t_{eqlb} near 200 h, suggesting that internal equilibration and outward diffusion are occurring simultaneously. Although differences in t_{eqlb} are observed among the experiments (Table 2), the high degree of overlap between the normalized release curves demonstrates a strong similarity in behavior and suggests that the differences in t_{eqlb} are not significant (Figure 4D).

[31] The individual experiment replicates are shown in Figure 4D to illustrate the largest source of error, which appears to be systematic in nature. For a given sample, the

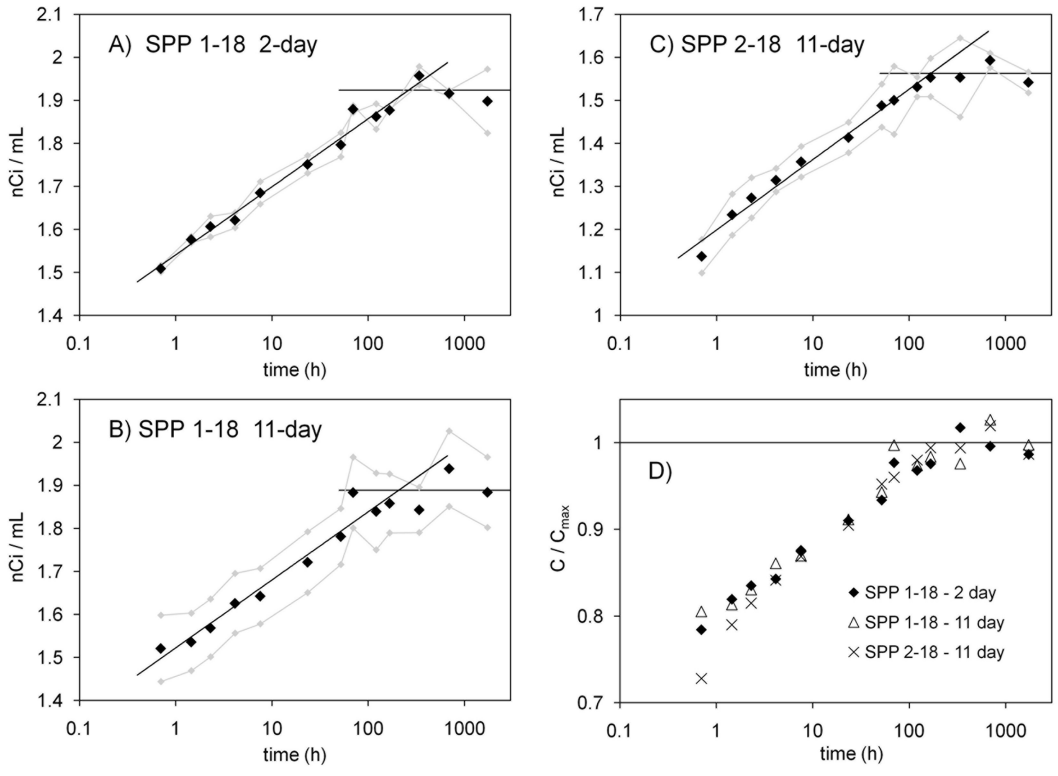

Figure 4. Tritium released from reacted sediments in the DB experiment, which involved vacuum drying and resuspension in a tritium-free solution. Aqueous tritium values are given as raw concentration in 4A–4C (gray lines are individual replicates, black diamonds are average values), which were normalized by the equilibrium concentrations (horizontal fitted lines) for the overlay in 4D.

two replicates showed very similar behavior with smooth, log linear increases to equilibrium, but the data were uniformly offset. This systematic error is likely because of a small difference in the amount of fine-grained material (and hence the total surface area) present in the two sample tubes, leading to slightly different overall capacities for tritium for the same sediment mass. Importantly, the differences are not a reflection on the uncertainty in kinetic behavior (see Appendix C).

[32] Tritium-hydrogen exchange site densities, *S*, were obtained from each batch experiment using the calculation procedure described in section 2. The *S* values obtained for sample SPP 1–18 exhibited no significant differences within error after pre-equilibration periods of 2 and 11 d, with an average value of 5.7×10^{-4} mol g^{-1}. The SPP 2–18 material exhibited a smaller *S* value (4.7×10^{-4} mol g^{-1}), which is consistent with the difference in BET surface area between the two materials (Table 1). On a BET surface area basis, the two materials have similar tritium-hydrogen exchange site densities near 19 sites nm^{-2}. These site densities fall within the range of values observed for various oxide surfaces [*Davis and Kent*, 1990; *Yates*, 1975; *Yates and Healy*, 1976] and for calculated values of surface hydroxyl site densities from crystal structures [*Koretsky*

Table 2. Calculation Results and Optimized Model Parameters for Tritium DB Experiments[a]

Sample	t_{eqlb} (h)	H^+ Exchange Site Density, *S*		K_E (H^+) (10^{-3} mL g^{-1})	Model Set B[b]		Model Set C[c]		
		(mmol g^{-1})	(sites nm^{-2})		μ	σ	f^{ig}	μ	σ
SPP 1–18 (2d)	263	0.574	19.3	5.18	−0.46	2.73	0.219	−2.29	1.66
SPP 1–18 (11d)	206	0.567	19.1	5.12	−1.51	2.16	0.198	−2.64	1.29
SPP 2–18 (11d)	168	0.466	18.6	4.20	−1.27	2.07	0.360	−1.02	2.19
SPP 2–16	–	0.53	19.0[d]	4.8	–	–	–	–	–
NPP 2–4	–	0.76	19.0[d]	6.9	–	–	–	–	–

[a]DB experiments were performed in duplicate, with average *S* and K_E values shown. Standard deviations for *S* and K_E were between 3% and 5.8% of the averages.

[b]Set B: DB-specific model refit of μ and σ after the odel set A optimization (set A parameters given in Table 3). f^{ig} and ε for set B are the same as in set A.

[c]Set C: DB-specific model refit of f^{ig}, μ, and σ. ε is the same as in set A (Table 3).

[d]DB experiments were not run on samples SPP 2–16 and NPP 2–4. *S* values (in sites nm^{-2}) were assigned as the average of the SPP 1–18 and SPP 2–18 values, and K_E values were calculated using this value.

et al., 1998], which can range from ~2 to >25 sites nm^{-2}. The similarity is encouraging, as it suggests that the dominant contribution to a hydrogen-tritium exchange is likely coming from chemisorbed/structural water (i.e., hydroxyls) on exposed (N_2 gas accessible) surfaces, rather than clay interlayers or residual physisorbed water on the sediment surfaces (see below). Since similar experiments were not performed using samples NPP 2–4 and SPP 2–16, S values on a mol g^{-1} basis were estimated for these samples assuming this average value (Table 2).

[33] Yates and Healy used a similar method to determine exchangeable proton site concentrations on silica and TiO_2 surfaces [*Yates and Healy*, 1976; *Yates et al.*, 1980]. By monitoring mass changes during drying using a microbalance and by comparison of sample preparations with and without heating, they determined that evacuation to <1 mTorr at room temperature was sufficient to remove all physisorbed water within 4 d [*Yates and Healy*, 1976]. Since our samples were exposed to <1 mTorr pressure for 7 d, the presence of residual physisorbed water on exposed, N_2 gas accessible surface area is believed to be insignificant. However, this does not rule out the possibility that some residual water within the clay interlayers remains after the drying procedure, thereby contributing to the observed tritium-hydrogen exchange. Mineralogical analyses of Hanford sediments have demonstrated the presence of clay minerals such as smectite (specifically, montmorillonite), muscovite, vermiculite, and chlorite [*Qafoku et al.*, 2005; *Serne et al.*, 2002]. However, it is difficult to know the exact percentages of the minerals contained within clay coatings, aggregates, and the loose clay fraction, and more importantly, the amount of interlamellar water retained after vacuum drying for 1 week in the DB experiment. For illustrative purposes, a rough approximation can be obtained by assuming an expandable-clay content of 1% by mass with montmorillonite as a model, based on a mineralogic analysis of sediment SPP 1–18 [*Qafoku et al.*, 2005]. Assuming the presence of one monolayer of intragranular water for an interlamellar water content of 120 mg H_2O g^{-1} of montmorillonite [*Mooney et al.*, 1952], this would yield a water-proton concentration (i.e., exchangeable hydrogen concentration) of ~ 0.13 mmol g^{-1} sediment, or ~20%–25% of the total measured tritium-hydrogen exchange capacity (Table 2). Although this fraction is substantial, it is very approximate and is very likely an overestimation, since the drying conditions employed here would likely leave submonolayer interlamellar water contents [e.g., *Vidal and Dubacq*, 2009 and references therein]. The implications of this uncertainty are discussed in more detail in Appendix C.

[34] The intra- and extragranular surface areas can be determined by multiplying the total (BET) surface area by the relative proportion of exchange sites in the intra- and extragranular zones (f^{ig} and f^{eg}, respectively). Although a more rigorous procedure for obtaining f^{ig} and intragranular pore volume from model fitting is presented in section 3.4, a simpler method can be used to obtain f^{ig} (required for estimating intragranular pore volume) directly from the DB data. We assume for this purpose that all of the tritium released before the first data point collected at 0.7 h after resuspension results from extragranular-region desorption, thus yielding an f^{eg} value of 0.78 ($f^{ig} = 0.22$). This number is the average of the $t = 0.7$ h data points in the SPP 1–18 and 2–18 11-d pre-equilibration experiments based on total tritium released (including tritiated water removed on sampling) rather than the aqueous concentration data shown in Figure 4. Note that the value of 0.78 is, in fact, an upper estimate on f^{eg}, since tritium on intragranular surface sites may have diffused out before 0.7 h. However, it can be considered a reasonable maximum value for the initial estimation of intragranular pore volume and surface area, particularly since some time would be required for sediment rehydration after extreme drying. Because of the strong similarity in behavior of the different sediments in both the DB and WB experiments, this f^{ig} value was assumed for all samples in the initial calculations.

3.3. Wet-Batch Tracer Release Results for Tritiated Water and Bromide

[35] The release-stage WB data for the four sediment samples studied were qualitatively similar to the DB data, exhibiting log linear tritium release before attaining equilibrium (Figure 5). A similar procedure was used to estimate the time required to reach equilibrium, whereby a line was fit to the log linear portion of the data and t_{eqlb} was taken as the crossing point of the log linear fit and the horizontal equilibrium line representing the average of the postequilibrium points. Values are given in Table 3 for comparison. For further comparison, the release curves are replotted in Figure 6 as the quantity of tritiated water released into solution after $t = 0$ (in nCi, which was corrected for sampling) per gram of sediment. Because the SPP 1–18 experiments were conducted using a smaller quantity of sediment but were pre-equilibrated under the same solid-to-solution ratio as the other samples (see section 2 for details), this is a more appropriate basis for comparison than raw concentration.

[36] The results suggest similar behavior for the SPP sediments after a long pre-equilibration, based on the strong degree of overlap in the release curves (Figure 6A). The t_{eqlb} values for these samples are within 230–350 h, with differences among samples that are probably not significant, given the similarity of the release curves. The NPP 2–4 curve, however, remains lower throughout much of the tritium release period and required a longer time to reach equilibrium (t_{eqlb} = 1000 h), suggesting a small difference in the rate limitation for this material but a similar capacity for tritium. For SPP1–18, unlike the DB experiments, pre-equilibration time made a very minor but noticeable difference in the tritium release; whereas the release curves exhibit strong overlap up to 100 h, a slightly greater quantity of tritium was ultimately released with a longer pre-equilibration. The 2-d experiment also required less time for equilibrium (t_{eqlb} = 190 h), but no difference in t_{eqlb} was observed between the 11- and 62-d experiments (~230 h for both). Given the similarity of the results obtained for sample SPP 1–18 equilibrated for 62 d and the other samples equilibrated for 7 months, this small pre-equilibration effect likely becomes unnoticeable after 2 months. However, it does leave open the possibility that a small difference may have been observed in the DB experiments had a longer equilibration time been used, despite the similarity between 2- and 11-d equilibrations.

[37] Intragranular pore volumes were calculated from the tritium WB results using equations (4)–(6) with f^{ig} = 0.22. The results were in a range of 2.8–3.6 mm^3 g^{-1}, representing 0.8%–1.0% of the sediment volume (Table 3). The

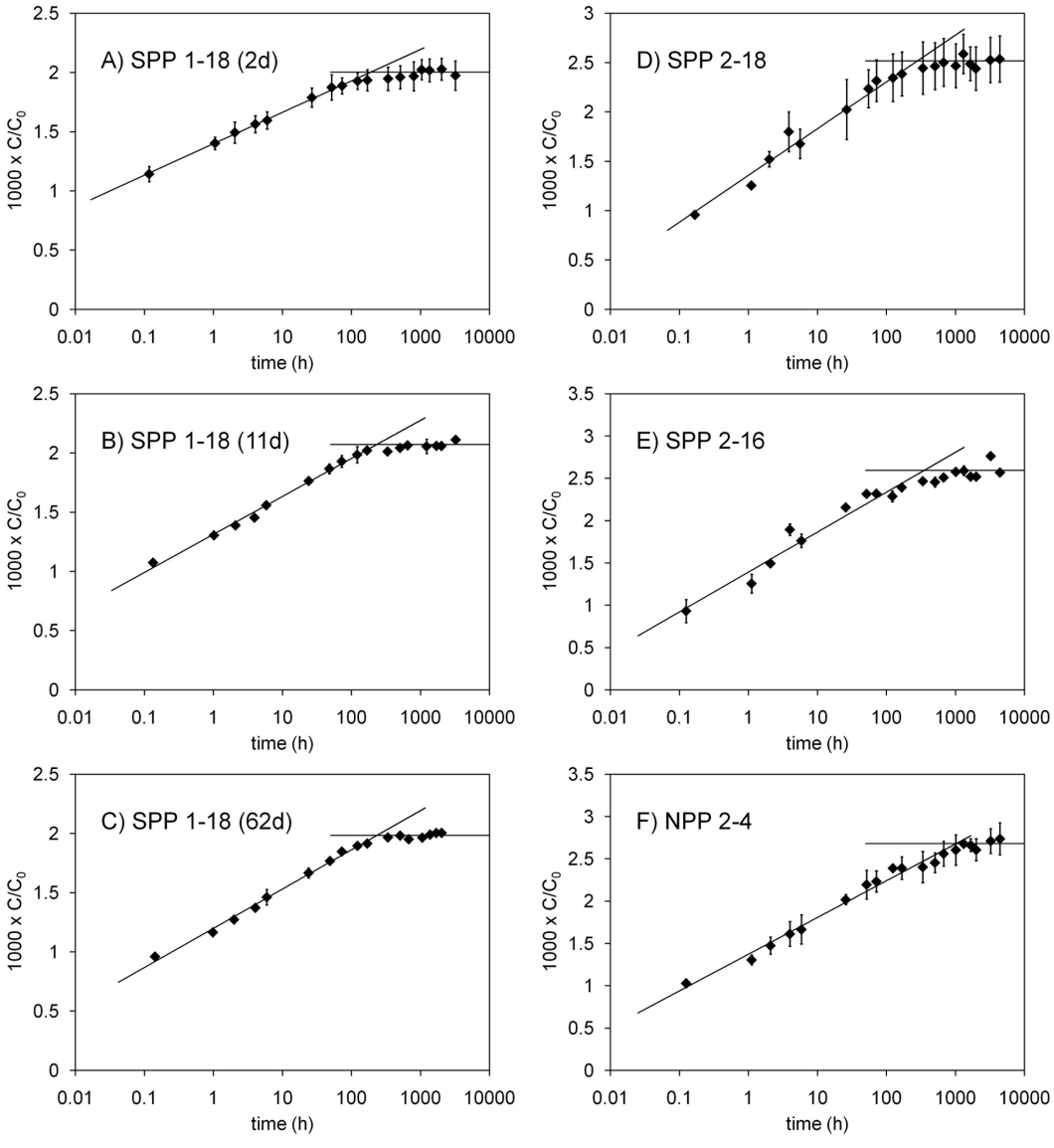

Figure 5. Tritium released in WB experiments for samples (A–C) SPP 1–18 as a function of pre-equilibration time (2, 11, and 62 d, respectively), (D) SPP 2–18, (E) SPP 2–16, and (F) NPP 2–4. Data are represented as aqueous concentrations normalized by represented as aqueous concentration normalized by the initial solution concentration at the start of the wash. Values are multiplied by 1000 to simplify the axis. Error bars represent the standard deviation of two replicates.

Table 3. Calculation Results and Optimized Model Parameters for Tritium WB Experiments

Sample	t_{eqlb}[a] (h)	V^{ig}[a] (mm^3 g^{-1})	ε[a] (%)	Model Set A[b]				Model Set D[c]		D/a^2 (d^{-1})
				f^{ig}	ε (%)	μ	σ	μ	σ	
SPP 1–18 (2d)	190	2.82 ± 0.49	0.79	0.343	0.534	−0.42	2.87	1.28	2.82	0.597
SPP 1–18 (11d)	231	2.98 ± 0.16	0.83	0.269	0.768	−1.48	2.69	0.62	3.22	0.194
SPP 1–18 (62d)	232	3.26 ± 0.10	0.91	0.265	0.880	−1.57	2.81	0.37	3.26	0.167
SPP 2–18 (7 mo)	278	3.56 ± 0.48	1.00	0.337	0.789	−1.23	2.98	−0.12	2.00	0.269
SPP 2–16 (7 mo)	351	3.55 ± 0.03	0.99	0.3	0.918	−1.26	2.99	−0.35	1.65	0.303
NPP 2–4 (7 mo)	1014	2.83 ± 0.23	0.79	0.3	0.678	−1.76	3.75	0.18	2.80	0.112

[a]Values calculated directly from the data are based on duplicate WB experiments, with the averages given. Numbers following ± are standard deviations between values calculated from the two experiments.
[b]Set A: Simultaneous fit to WB (release stage only) and DB data as described in the text.
[c]Set D: Model fit to the full WB data set (washing + release stage data) with $\varepsilon = 2\%$.

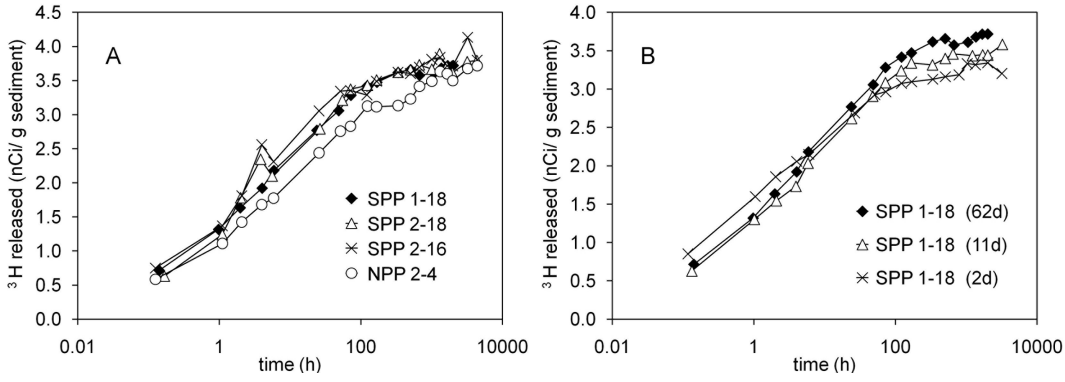

Figure 6. Tritium released in the WB experiments, replotted from Figure 5 as the quantity of tritium released per gram of sediment and corrected for sampling. (A) An overlay of the results obtained for the four different samples under the longest pre-equilibration times tested. (B) An overlay of the SPP results obtained for different pre-equilibration times.

differences observed among SPP 1–18 experiments followed the tritium release trends with the pre-equilibration time noted above, with values ranging from 2.8–3.3 mm^3 g^{-1} ($\varepsilon = 0.8\% - 0.9\%$) depending on the amount of tritium taken up and ultimately released. Among the long pre-equilibration experiments, the largest observed differences followed trends in the proton exchange K_E value (largely controlled by the BET surface area) owing to the large contribution of tritium released from exchange sites in the intragranular region. This effect is most noticeable for NPP 2–4; because the overall quantity of tritium taken up and released was very similar for NPP and SPP sediments (Figure 6A), the larger proton exchange K_E value assumed for NPP 2–4 resulted in a relatively low V^{ig}.

[38] Bromide ion (Br^-) exhibited strikingly different behavior than tritiated water in batch experiments. Bromide WB release results obtained after 2- and 65-d pre-equilibration times are shown in Figure 7, represented as nmol of Br^- released from time $t = 0$ g^{-1} of sediment. The experiment replicates are plotted individually, rather than averaged. As with the tritium results in Figure 5, the calculation of $t > 0$ release required subtraction of the quantity of Br^- remaining in the bulk solution after the final wash. In the case of Br^-, the calculated $t = 0$ solution concentration was higher than the first measured concentration at $t \sim 0.1$ h, causing Br^- release curves to drop below zero. Bromide release also came to equilibrium much more quickly, with the release curves leveling off between 1 and 10 h. Given the lack of reproducibility between replicates, the data cannot be used to obtain a reliable estimate of the intragranular pore volume.

[39] One possible explanation for the observed behavior of Br^- is anion exclusion by negatively charged sediment pore surfaces (Figure 1i) [e.g., *Appelo and Wersin*, 2007; *Demir*, 1988; *Liu*, 2007], which may include oxides (e.g., Fe-oxides and silica) with point of zero charge (PZC) values lower than the experimental pH of 8.65 and the surfaces of permanently charged aluminosilicates, which may occur as aggregates and coatings on grains [*Stubbs et al.*, 2009; *Zhang et al.*, 2011], and possibly within quartz and feldspar grain fracture walls in sandy aquifer sediments [*Wood et al.*, 1990]. Anion exclusion would be theoretically possible; the experimental ionic strength of 0.0114 yields a Debye length of ~2.9 nm, which is comparable to the radii of pores probed in this study. Anion exclusion would be expected to reduce the quantity of Br^- that would

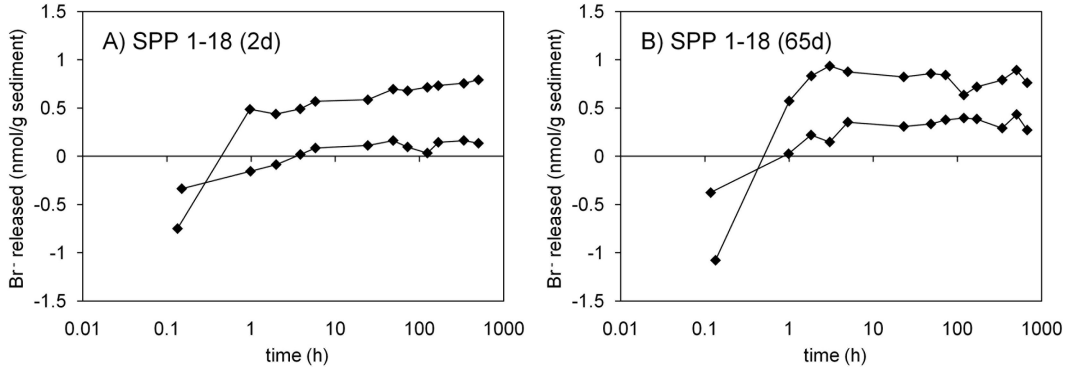

Figure 7. Bromide released from reacted WB-experiment sediments, plotted as quantity released from time $t = 0$ per gram sediment and corrected for sampling as described in the text. The $t = 0$ concentration, calculated on the basis of the dilution of the residual solution by the backfilled volume, was greater than the first measured value, resulting in the negative values at $t = 0.1$ h. Data for two sample replicates, each for SPP 1–18 2-d (A) and SPP 1–18 65-d (B) experiments, are plotted.

diffuse into intragranular pores, resulting in a smaller observed intragranular pore volume. Here the effect may also be from excluding Br^- from the pore space between the grains of sediment at the bottom of the tube on centrifugation, leaving a higher concentration of Br^- in the supernatant; a greater proportion of Br^- would be removed on washing, resulting in an overprediction of $C^{eg}_{t=0}$ calculated by dilution, thus causing the curves to drop below zero. Although consistent with the observation, the bromide method lacks the necessary reproducibility and sensitivity to be able to confirm this hypothesis.

3.4. Mass Transfer Modeling

[40] A multirate first-order mass transfer model was applied to the tritium release data in order to further characterize and quantify the release rates and to provide an alternate means of estimating intragranular pore volume from the data. Rate coefficients in the multirate model could be chosen independently, but are generally assumed to follow a distribution in order to minimize the number of adjustable parameters [*Culver et al.*, 1997; *Haggerty and Gorelick*, 1995]. Here we assume a lognormal distribution of rate constants, which is a very common choice generally [*Culver et al.*, 1997; *Pedit and Miller*, 1994] and specifically in Hanford 300A studies [*Greskowiak et al.*, 2011; *Liu et al.*, 2008, 2009; *Ma et al.*, 2010]. The advantage of the distributed-rate model over an explicit diffusion model is that it is a relatively simple model, with few parameters, that is capable of describing kinetics in highly complex, heterogeneous systems, where diffusion may be occurring within grains of different sizes, in clay coatings of varying thicknesses, and within intragranular pores of nonuniform pore connectivity within the grain.

[41] In preliminary attempts to fit the rate distribution parameters μ and σ to the WB and DB data sets, it was observed that the DB fits were more sensitive to adjustments in f^{ig} than in ε; whereas in the WB fits (excluding the washing data), f^{ig} and ε exhibited a strong inverse correlation. This is not surprising; in the DB model, the initial intragranular region concentration is entirely dependent on the choice of f^{eg} (and hence f^{ig}), but a good fit to the data can be obtained for a wide range of f^{eg} by adjusting the rate parameters to control the quantity of tritium released before the first data point near $t = 0.7$ h. In this way, f^{ig} exerts a stronger control on the rate parameters than ε; it also means that obtaining a unique value of f^{ig} from the DB data alone is difficult. In the WB model, however, the extragranular concentration at $t = 0$ is much less sensitive to f^{eg}; it is almost entirely controlled by the tritium remaining in bulk solution at the end of the wash. In this case, f^{ig} is important in controlling the initial amount of tritium in the intragranular region, but this effect is balanced by the choice of ε to accurately model the total amount of tritium released from the intragranular region after the washing stage.

[42] Since the DB data could be modeled with a wide range of rate distribution parameters depending on f^{ig}, it was possible to find a set of μ, σ, f^{ig}, and ε values that described both the WB and DB data sets for a given material. In this procedure, initial estimates of μ, σ, and ε were obtained by fitting the WB data with $f^{ig} = 0.22$. (This first calculation invariably yielded the same ε values that were calculated previously, since the same assumptions went into determining those values.) Using the fitted μ, σ, and ε values, a model fit to the DB data was then obtained by adjusting f^{ig} only. This updated f^{ig} value was used to refit the WB data, and the cycle was repeated until convergence was achieved. This procedure had the added advantage of constraining f^{ig}, which could not be determined uniquely from the DB data alone. However, the procedure assumes that the tritium release rates would be the same in both experimental schemes (see Appendix C).

[43] This fitting procedure was conducted for the available WB-DB data set pairs, including the SPP 1–18 2- and 11-d pre-equilibration sets, as well as for the SPP 1–18 and SPP 2–18 long pre-equilibration WB data using the corresponding 11-d DB data. Since corresponding DB data were unavailable for SPP 2–16 and NPP 2–4, an average f^{ig} value was used to obtain WB model fits. These results are listed in Table 3 as model set A. The fitting procedure yielded f^{ig} values between 0.27 and 0.34, higher than the 0.22 assumed in the calculations above. Accordingly, the larger f^{ig} values resulted in lower fitted ε values of 0.53%–0.92% in order to conserve mass in the intragranular region.

[44] An example of the fitting results is shown in Figure 8 for the SPP 1–18 (11-d) experiments, illustrating that both WB and DB data are well-described using the lognormal distributed-rate model, and that reasonable fits can be obtained using the same distribution parameters for both experiments (solid black curves, Figures 8A and 8B). However, since μ and σ were obtained by fitting the WB release curve only, these are technically not the values that would be obtained if these parameters were allowed to vary during the DB optimization. For comparison, DB fits were also obtained by keeping f^{ig} and ε constant at the optimized values and adjusting μ and σ (dotted line, Figure 8B; model set B, Table 2) and by adjusting f^{ig}, μ, and σ (dashed line, Figure 8B; model set C, Table 2). Although the adjustable parameters showed some change on reoptimization with a decrease in the residual (e.g., for SPP 1–18 11 d: 23% decrease from set A to B, 40% decrease from A to C), the cosmetic fit to the data did not improve substantially, further suggesting that the original fit based on WB and DB results is adequate.

[45] Results from the WB experiments were also modeled by including data collected throughout the washing stage. Convergence of the fitting parameters could not be achieved when the washing data were included, likely because of the assumptions required for their incorporation in the model. These details and the fitting results are discussed in Appendix A.

[46] The disadvantage of the distributed-rate model is that the rate parameter α (and therefore μ and σ) lacks intuitive physical meaning. For comparison with the mass transfer fittings, and to obtain an average value of the physical diffusion rate within the intragranular zone, a spherical diffusion model was also used to describe the WB results. This model was fit to the data by optimizing the lumped parameter D/a^2, with f^{ig} and ε fixed according to their mass transfer model Set A values (Table 3). The fit to the SPP 1–18 11-d WB data set is shown in Figure 8A. The data clearly show a greater spread in diffusion rate than is predicted by the simple (single-radius, uniform porosity) spherical diffusion model, since tracer release from the sample is

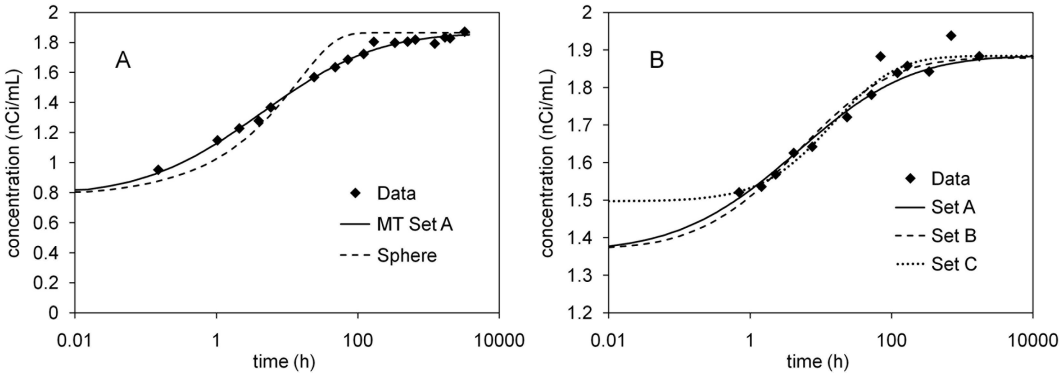

Figure 8. (A) SPP 1–18 11-d WB experiment with mass transfer model set A (simultaneous WB-DB fit) and spherical diffusion model fits. (B) SPP 1–18 11-d DB experiment results with mass transfer model set A fit (simultaneous WB-DB fit, solid line), set B fit (reoptimization of μ and σ; dotted line), and set C fit (reoptimization of μ, σ, and f^{eg}; dashed line).

governed by a more complex diffusive domain (e.g., spheres of different radii, grain coatings, and nonuniform particle porosity/pore connectivity). Regardless, the fitted D/a^2 value can be thought of as corresponding to an "effective" spherical particle representing the average diffusive properties of the sediment grains. For illustration, we take $a = 1$ mm (the actual particle size varies between 0 and 2 mm) and an average D/a^2 value for all the samples of 0.27 d^{-1} (Table 3). This yields a diffusion coefficient for tritiated water on the order of 3×10^{-12} m^2 s^{-1} within the intragranular domain, which is about three orders of magnitude slower than the diffusion rate of HTO in free water (2.24×10^{-9} m^2 s^{-1} at 25°C) [*Mills*, 1973], suggesting very high tortuosities for tritiated water within the immobile zone. *Ball and Roberts* [1991] observed a similar two to three orders of magnitude difference between bulk and intragranular diffusion rates for chlorinated organics within the intragranular zone of Borden sand.

3.5. Comparison of N_2 Gas Adsorption and Tritium Mass Transfer Results

[47] The tracer results may be compared with the porosity and surface area distributions obtained from N_2 gas adsorption. To do this, however, one must assume that the intragranular pore volume measured in the tracer studies corresponds to the narrowest subset of pores measured by gas adsorption. This is not necessarily the case; it is possible that complex pore network connectivity results in a poor correlation between pore size and diffusion limitation. In other words, some mesopores might have a larger diffusion limitation than many micropores depending on where they are in the intragranular network and their accessibility to the grain surface. A comparison between gas adsorption and tracer diffusion results is therefore informative, but imperfect.

[48] The pore volumes obtained from the tritium release experiments (model set A values) were compared with their respective desorption *t*-plot analysis results (Table 4). Since the desorption curve includes contributions from large pores affected by small pore necks, it is assumed to more closely represent the diffusion-limited pore space, as tracer diffusion would also be controlled by the width of pore openings. For the SPP samples, the comparison suggests that the intragranular pore volume probed using the tritium tracer method includes all of the pores of width less than 0.6 nm, as well as a portion of the volume controlled by pores/pore necks with width greater than 0.6 and less than the Kelvin cutoff (2.4–3.6 nm). Table 4 lists the fraction of V^{ig} accounted for by <0.6 nm pores. For the SPP sediments, 38%–50% of V^{ig} falls within this fraction, while for NPP 2–4, V^{ig} is entirely accounted for by <0.6 nm pores. Interestingly, the *t*-plot < 0.6 nm pore volume for this sample was significantly higher than for the SPP sediments, while its capacity for tritium uptake and release (i.e., V^{ig}) was not significantly different.

[49] A similar comparison was made between the *t*-plot and tracer-analysis intragranular surface areas. The percentage of A^{ig} (intragranular surface area estimated from tracer release) contained within <0.6 nm pores is slightly higher than the percentage of V^{ig} contained within these pores for the SPP sediments, but not for NPP 2–4. This result is

Table 4. Pore Volumes and Surface Areas from Tritium Tracer Release and N_2 Gas Adsorption

	Pore Volume Comparison (PV, mm^3 g^{-1})			Surface Area Comparison (SA, m^2 g^{-1})		
Sample	^3H V^{ig}	<0.6 nm[a]	0.6 nm–Kelvin Cutoff[b]	^3H A^{ig}	<0.6 nm	0.6 nm–Kelvin Cutoff
SPP 1–18	3.14	1.57 (0.50)	8.36	4.75	3.54 (0.74)	5.69
SPP 2–18	2.82	1.08 (0.38)	8.48	5.09	2.18 (0.43)	5.92
SPP 2–16	3.28	1.32 (0.40)	8.45	5.04	2.73 (0.54)	5.56
NPP 2–4	2.45	2.57 (>1.0)	9.11	7.25	5.70 (0.79)	7.60

[a] *t*-plot pore volumes/surface areas of pores with width <0.6 nm. Numbers in parentheses give the fraction of V^{ig} (or A^{ig}) accounted for by the *t*-plot values.
[b] *t*-plot pore volumes/surface areas of pores with width between 0.6 nm and the Kelvin cutoff (2.4 nm for slit-pores, 3.6 nm for cylindrical pores).

surprising; one would expect that the surface area percentage would be much higher than the volume percentage for the narrower pores, given their higher surface area-to-volume ratio. This might suggest a weakness in the comparison between gas adsorption and tracer diffusion results, as mentioned above. (For example, it is possible that some of the micropore volume is close enough to the mineral surfaces as to provide a minimal diffusion limitation.) A more important factor might be the questionable validity of estimating the micropore surface area as the difference between the external *t*-plot and BET areas. Both of these weaknesses highlight the need for a "diffusion-based" method of obtaining intragranular pore volume and surface area for transport applications.

4. Conclusions

[50] In this study, tracer uptake and release experiments were performed to characterize the diffusive properties of the intragranular porosity regime within sediment grains and aggregates, including pore volumes and rates of mass transfer between intra- and extragranular regions. The method was developed and tested using U(VI)-contaminated sediments collected from the vadose and seasonally saturated zones beneath former waste processing ponds in the Hanford 300 Area, where sorption sites within intragranular pore spaces exert a strong control on the reactive transport of uranium.

[51] Tritiated water was found to be an ideal tracer for these studies, as it is an accurate, unbiased, high-resolution probe of solution-phase behavior. In most applications studying bulk water transport in the presence of macroporosity, the transport of tritiated water is not affected in major ways by the comparatively small fraction of hydrogen that is bound to surface sites. In probing the small solution volumes present in the intragranular zone, however, the quantity of exchangeable surface-bound hydrogen was significant, making tritium a useful surface probe in our experiments as well. In this study, different batch experiment techniques (termed the "wet-batch" [WB] and "dry-batch" [DB] methods) were used to distinguish aqueous-phase and surface-bound tritium, as well as the relative proportions of intra- and extragranular surface-exchanged tritium. By utilizing these complementary techniques, both intragranular pore volumes and fraction of total surface area within the intragranular region could be estimated from the tracer release results. Two methods were provided for obtaining intragranular pore volumes and surface areas; one involving direct calculation based on mass balance considerations, and the other involving fitting of a mass transfer model. Tritium release from the intragranular zone in both WB and DB experimental schemes was well-described using a distributed-rate first-order mass transfer model with a lognormal distribution of rate constants. Because of the differential sensitivities of the WB and DB results to the model parameters, it was possible to find a single set of parameters that fit both data sets for a given sample, thus providing a more rigorous, self-consistent estimate of the intragranular sorption site fraction (f^{ig}) than a direct estimation from the DB data.

[52] The intragranular pore volume estimates obtained for the Hanford 300A sediments suggest that intragranular porosity is small, representing ~1% of the sediment skeletal volume. Although this would account for a small portion of the total porosity within a packed column (e.g., 1.5% for a column porosity of 0.4 [*Liu et al.*, 2008; *Qafoku et al.*, 2005]), the intragranular pore space clearly contains a significant portion of the surface area (~20%–35%) and hence a significant portion of the total ion sorption sites. We therefore expect that for this system and other systems with similar grain-scale characteristics, the transport of adsorbing solutes would be strongly affected by the presence and diffusive characteristics of the intragranular zone, even while its effect on nonsorbing solutes may be hardly noticeable. The results obtained using bromide as a tracer, although consistent with an anion-exclusion mechanism limiting the concentration of bromide within the intragranular pore space, were ultimately inconclusive due to a lack of strong reproducibility. Although bromide results are thus insensitive at detecting or characterizing intragranular porosity, the tritiated water results (and the comparison of these results with bromide) serve to highlight the important role of intragranular porosity and surface reactions on solute transport.

[53] A comparison of the tritiated water results, with surface areas and porosities estimated from *t*-plot analyses of N_2 gas adsorption and desorption, indicates that the tracer-derived intragranular pore volumes include pore sizes that fall in the traditional "micropore" (<2 nm) and "mesopore" (2–50 nm) classifications, falling within a pore size regime that is below the tensile-strength limit of condensed N_2, (2.4–3.6 nm). However, this comparison is based on the assumption that pore size and diffusion limitation are correlated. Although the N_2 gas adsorption method is useful in this pore size range, relating the results to transport-relevant parameters is difficult in the presence of complicated pore network effects. In comparison, Hg-intrusion porosimetry, which requires very high operating pressures in the low mesopore range and cannot access pores below 3 nm diameter under reasonable pressures, is of very limited usefulness in this pore size range, further highlighting the need for a complementary, kinetic-based method of estimating intragranular porosity and surface area. Here we demonstrate a method that is based on tracer diffusion, making it more directly applicable to problems of mass transfer-limited reactive contaminant transport.

Appendix A: Calculation of v^{ig} With and Without Inclusion of "Washing-Stage" Data

[54] The mass balance equation for tritium in the WB experiments is given by

$$q_{rel} = -\Delta q^{ig}_{aq} - \Delta q^{eg}_{\text{surf}} - \Delta q^{ig}_{\text{surf}}, \tag{A1}$$

from which we can calculate v^{ig}. Assuming that the tritium-hydrogen exchange reaction occurs rapidly in both the intra- and extragranular regions, this yields

$$\begin{aligned} q_{rel} = {} & \left(C_i - C_f\right) m V^{ig} + \left(C^{eg}_{t=0} - C_f\right) f^{eg} m K_D \\ & + \left(C_i - C_f\right) f^{ig} m K_D, \end{aligned} \tag{A2}$$

where q_{rel} is the moles of tritium released into the extragranular region (i.e., the change in moles of tritium in the

extragranular region between $t = 0$ and $t = t_{eqlb}$), C_i is the aqueous tritium concentration after pre-equilibration and before washing, C_f is the final tritium concentration after release (taken as the average of numerous points after equilibrium has been reached), and V^{ig} is the intragranular pore volume per unit sediment mass. q_{rel} is calculated as

$$q_{rel} = q^{eg}_{aq,f} - q^{eg}_{aq,t=0} + q_{samp}, \quad \text{(A3)}$$

where $q^{eg}_{aq,t=0}$ and $q^{eg}_{aq,f}$ are the moles of tritium in the extragranular region aqueous phase at $t = 0$ and $t > t_{eqlb}$, respectively, calculated from aqueous concentrations at these respective times.

[55] $C^{eg}_{t=0}$ (the open diamond at $t = 0$ in Figure 2A) is calculated by dilution of the last known aqueous concentration during the wash, corresponding to the supernatant removed after the final centrifugation step, accounting for extragranular region desorption. This dilution calculation was performed based on the quantity of extragranular water present in the experiment before and after backfilling, estimated based on the amount of solution added and removed at each step, plus the amount of hydration water present on the sediment under air-dried conditions, minus the intragranular pore volume. Thus, in order to calculate intragranular pore volume, an initial guess for V^{ig} was needed. In the calculation, the initial intragranular volume was adjusted iteratively until it matched the calculated value.

[56] This intragranular pore volume calculation only considers the tritium released from the intragranular zone during the release stage of the experiment. The procedure therefore ignores the tritiated water that diffuses out of intragranular pore space during most of the washing stage. An attempt was made to include washing data in the calculation of V^{ig}, but inclusion of these data led to nonconvergence on the V^{ig} iteration described above. Specifically, the diluted (calculated) concentrations in the washing stage are so strongly dependent on the V^{ig} assumption that the calculated V^{ig} becomes entirely dependent on the assumed value, such that V^{ig} does not converge on iteration.

[57] It was possible, however, to include the washing-stage data in the mass transfer modeling. The model results are shown for the SPP 1–18 long pre-equilibration experiment in Figure A1 for a variety of parameter values. When the parameters obtained without washing data are applied to the full data set, the resulting model curve underpredicts the amount of tritium released in the release stage (the gray line, Figure A1B). This is as expected, since a portion of the tritium that was released in the early release stage is now being released into bulk and removed from the system during the wash. Reoptimization of μ and σ while holding f^{eg} and ε constant brought some of the mass back into the release stage (dotted line, Figure A1B), but did not provide an adequate model fit, suggesting an underestimation of ε using the release data alone. Significant improvements in the model fits were obtained by allowing ε to increase, but in all of the samples, model optimization on ε, μ, and σ did not lead to convergence within any reasonable range of ε. This is apparently largely because of the inability of the

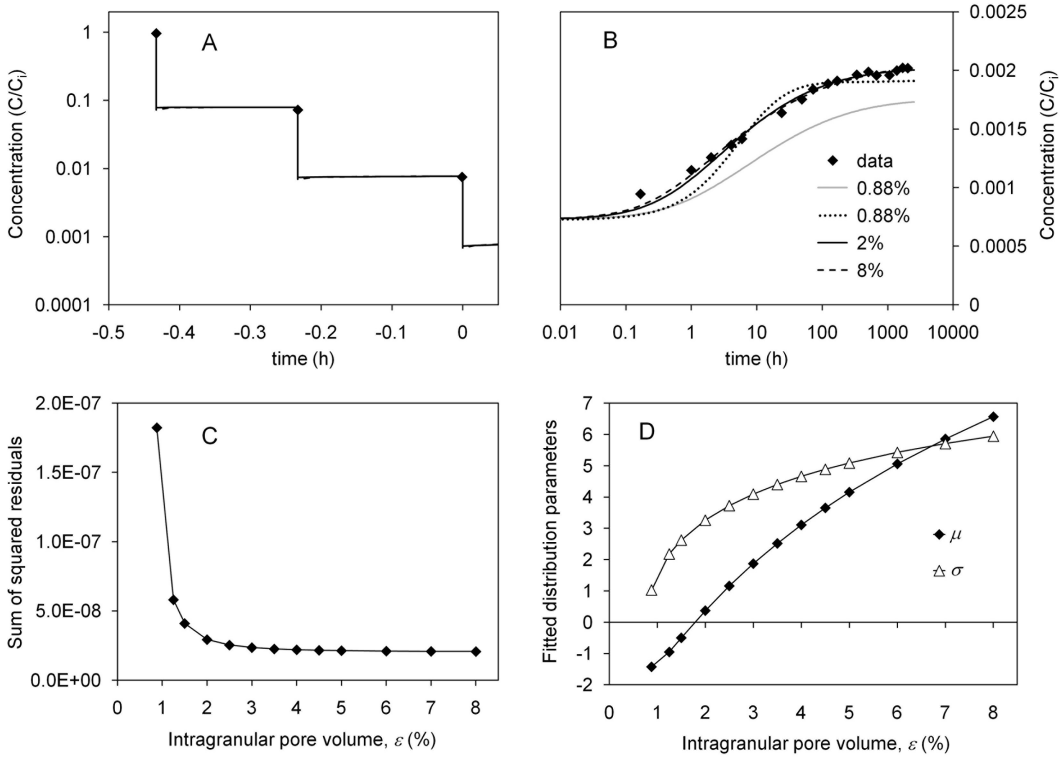

Figure A1. SPP 1–18 62-d experiment results and model fits to the full data set, including wash and release-stage data (A and B, respectively). The legend in B gives the ε value corresponding to the fit; other details are described in the text. Because convergence was not achieved when ε was allowed to vary in optimization, the model was optimized at fixed ε values, with the sum of squared residuals, μ, and σ values given in C and D as a function of ε.

model to reproduce the sharp increase in tracer concentration observed for the first data point at $t \sim 0.1$ h. When washing data are not included, this early release is easily described by tracer present in rapidly exchanging intragranular domains, but when the washing data are included, these domains are depleted. Further increases in ε and μ only cause more tracer to be released in the washing stage, with minimal effect on the release-stage profile. This diminishing return on increasing ε can be seen in Figure A1C, which shows the sum of squared weighted residuals between data and model points in the release stage for sample SPP 1–18 (62 d) as a function of ε. A substantial decrease in the residual is obtained by increasing ε from 0.88%, but little improvement is observed above 2%–2.5% as ε, μ, and σ are increased further (Figures A1C and A1D). This can also be seen in Figures A1A and A1B, where the optimized model outputs for $\varepsilon = 2\%$ (solid black line) and $\varepsilon = 8\%$ (dashed line) are overlaid. Despite the fourfold increase in ε, only very small differences can be observed in the release stage. (Differences are more substantial in the washing stage, but are difficult to see in Figure A1A due to the log-concentration scale.) Since convergence could not be obtained by including ε as an adjustable parameter, model fits were obtained by adjusting μ and σ with $\varepsilon = 2\%$ (model set D, Table 3).

[58] A very likely possibility for this lack of convergence is that the inclusion of the washing-stage data under the given modeling assumptions tends to strongly overestimate tracer release. Specifically, the model assumes that resuspension of the sediment occurs instantaneously after the addition of tracer-free solution during each wash cycle, as shown schematically in Figure 2 and by the model results in Figure A1A, and that mass transfer can freely occur between the extra- and intragranular regions between each addition of tracer-free solution. However, the sediment is actually present for the majority of the washing stage as a dense plug at the bottom of the reaction vessel, as the time between the additions of tracer-free solution is required for centrifuging and decanting. Tracer diffusing from the intragranular region is not released into a well-mixed bulk solution, but rather into the small pore volume between grains within the compacted sediment plug. Released tracer is diluted to a lesser degree, leading to a weaker driving force for mass transfer. Another possibility is that the data are in fact not well-described using the lognormal rate distribution; it is possible that an asymmetric or bimodal distribution might improve the description of the tracer release in the early release stage. Attempts to fit the data using a simple two-rate mass transfer model (results not shown) support this hypothesis.

Appendix B: Comparison of N_2 Gas Adsorption Microporosity Methods

[59] For comparison of gas adsorption isotherms and validation of the *t*-plot method, a N_2 sorption isotherm was recollected for sample SPP 1–18 on an instrument capable of achieving lower relative pressures. Within the overlapping pressure range, the isotherms and *t*-plot results obtained were identical for both instruments. Use of the lower-pressure instrument enabled the application of additional micropore analyses, including the Horváth-Kawazoe (HK) [*Horváth and Kawazoe*, 1983] and Saito-Foley (SF) [*Saito and Foley*, 1991] micropore size-distribution methods. The two methods are very similar; the primary difference is that the HK method assumes a slit-shaped pore geometry, while the SF method assumes cylindrical pores. Both methods assumed gas adsorption on an aluminosilicate-type surface.

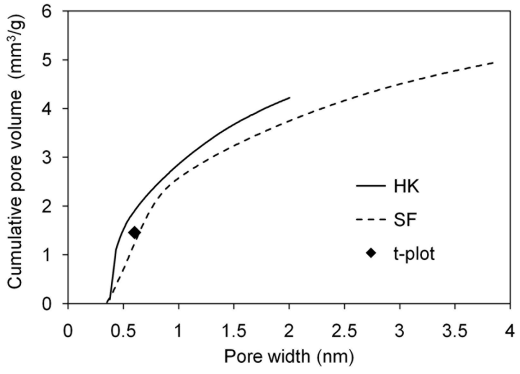

Figure B1. Micropore volumes obtained using the Horvath-Kawazoe, Saito-Foley, and *t*-plot methods.

[60] The cumulative pore volumes obtained using these methods applied to the adsorption isotherm are shown in Figure B1, compared against the <0.6 nm *t*-plot pore volume. Good agreement is obtained between the three methods near 0.6 nm with the *t*-plot value falling in between the HK and SF predictions, illustrating that 0.6 nm is a good assumption for maximum pore width in the *t*-plot interpretation. The strong agreement between the three methods lends support to the validity of the low-range *t*-plot analyses applied to the other samples studied.

Appendix C: Assumptions Required and Uncertainty in the Estimation of V^{ig} and A^{ig}

[61] It is assumed that the amount of tritium released during the WB washing stage is minimal, thus allowing us to ignore this data in the calculation of V^{ig}. This assumption was necessary given the problems associated with including this data in the calculations (discussed in detail in Appendix A). In fact, it is expected that some tracer does diffuse out of the intragranular zone during the wash, but the analysis in Appendix A suggests that this release will not be as much as what one would predict for a well-stirred batch system throughout the entire washing period, since the sediment is compacted at the bottom of the tube for the majority of this time. Regardless, this assumption does result in an uncertainty in $C^{ig}_{t=0}$, which leads to uncertainty in V^{ig} (see below).

[62] The initial estimates of f^{eg} and f^{ig} assumed that the fraction of sorption sites residing in the extragranular zone corresponds to the fraction of tritium released by the first data point ($t = 0.7$ h) in the DB experiment. As discussed in the text, this assumption effectively yields a minimum estimate of f^{ig}, since some tritium will have diffused out before $t = 0.7$ h. In the mass transfer modeling technique, f^{ig} values are determined that are consistent with WB and DB data sets. In this case, f^{ig} is taken as the model-extrapolated intragranular fraction of tritium at $t = 0$ and is thus likely a more reasonable estimate. However, the simultaneous WB-DB model fitting procedure assumes that any kinetic

differences resulting from the differing experimental techniques (e.g., the time required for rehydration in the DB approach) are minimal, such that model parameters would be the same for both. The overall difference between maximum and minimum f^{ig} (and hence f^{eg}) values determined in this work was 0.12, which represents ~17% of the average f^{eg} and ~42% of the average f^{ig}.

[63] A third assumption required in the calculations was that all physisorbed water was removed during the drying step in the DB experiments, leaving only surface-bound (chemisorbed, hydroxyl-exchanged) tritium. Although this assumption is reasonable for adsorbed water on external surfaces, the amount of water remaining in clay interlayers is unknown, though likely small (see the discussion in section 3.2). This assumption may therefore lead to an overestimation of K_E, which we estimate to be ~25% at most. This is in addition to the relatively large measurement uncertainty observed in Figure 4. The uniform offset between measurement replicates, while not affecting kinetic analyses, reflects experiment error in the total sorbed tritium quantity (i.e., K_E). The maximum error in K_E was observed for the SPP 1–18 11-d experiment, with one standard deviation representing ±6%.

[64] The calculation of V^{ig} will therefore be most affected by uncertainties in $C^{ig}_{t=0}$, f^{ig}, and K_E. Although there is also a large uncertainty associated with the assumed value of 2.8 for the sediment skeletal density ρ, this value is not used in the calculation V^{ig}, only in estimation of ε from V^{ig}. (There is therefore an uncertainty in ε proportional to the uncertainty in ρ, but for all ε values reported in the tables, this uncertainty is removed on conversion to V^{ig} with $\rho = 2.8$.) The sensitivity of V^{ig} to these uncertainties was determined empirically by adjusting the independent variable within a given percentage range and observing the change in V^{ig}. The results are summarized as follows:

$$\frac{\delta V^{ig}}{V^{ig}} = B_1 \frac{\delta K_E}{K_E},\ B_1 = -0.3 \text{ to } -0.7 \text{ for } K_E \pm 2 \text{ to } 30\%; \quad \text{(C1)}$$

$$\frac{\delta V^{ig}}{V^{ig}} = B_2 \frac{\delta f^{ig}}{f^{ig}}, B_2 = -0.3 \text{ to } -0.7 \text{ for } f^{ig} \pm 2 \text{ to } 50\%; \quad \text{(C2)}$$

$$\frac{\delta V^{ig}}{V^{ig}} = B_3 \frac{\delta C^{ig}_{t=0}}{C^{ig}_{t=0}},\ B_3 = -0.9 \text{ to } -2.4 \text{ for } C^{ig}_{t=0} \pm 2 \text{ to } 30\%. \quad \text{(C3)}$$

For example, an increase in the K_E value of 10% would yield a decrease in V^{ig} as large as 7%, depending on the sample. The B coefficients determined represent the ranges of values observed for all samples studied and are specific to the sample properties and experiment conditions used here. The wide ranges result from the fact that sensitivity to one variable is dependent on the values of other variables; as such, the errors are not strictly additive. As an extreme case, V^{ig} was calculated with a simultaneous 30% adjustment in K_E, f^{ig}, and $C^{ig}_{t=0}$. Increasing each of the three values by 30% caused a decrease in V^{ig} of 50%–88%, and decreasing each by 30% caused an increase in V^{ig} of 70%–110%. Although these uncertainties in V^{ig} are conservatively high (the errors assumed for each value are on the high end and in reality will not likely affect V^{ig} in the same direction), it illustrates the degree to which the uncertainty in these variables affects the estimation of V^{ig}. Uncertainty in $C^{ig}_{t=0}$ is found to most strongly affect V^{ig}, while also being the more difficult uncertainty to quantify. However, this uncertainty will affect the fast-diffusion intragranular regions more strongly than slow-diffusion regions. In this way, it may be useful from a practical perspective to consider the calculated V^{ig} an operational estimate that emphasizes intragranular zones under strong kinetic control.

[65] The uncertainty in A^{ig} is relatively straightforward. If one accepts that proton exchange sites are uniformly distributed across the surface (or at least uniformly partitioned between intra- and extragranular zones in proportion to surface area), then A^{ig} can be assigned as the product of f^{ig} and the BET surface area. The uncertainty in A^{ig} is then the sum of the uncertainty in these two values. In this study, the standard deviations between BET replicates happened to be <1%, but if the offset in DB replicates (Figure 4) can be attributed to surface area measurement uncertainty, then this deviation can be as high as ±5%.

[66] One final assumption worth noting, although it only affects the interpretation of diffusion rates and not the estimation of V^{ig} or A^{ig}, deals with the distribution of surface area within the intragranular region. Specifically, it was assumed in this study that the surface area (and therefore sorption/exchange site density)-to-pore volume ratio is constant throughout the intragranular region, and thus independent of rate coefficient. This is not necessarily the case; for example, one might reasonably expect that relatively narrow pores would exhibit both slower mass transfer rates and higher surface area to volume ratios than wider pores. This could be modeled by increasing the sorption site densities for intragranular subdomains with smaller rate coefficients. In actuality, the relation between diffusion rate and surface area-to-volume ratio is not that simple, as mass transfer rates are also controlled by pore length (which itself does not affect surface area to volume ratio) and complex pore geometries and networks (e.g., large pore bodies controlled by narrow pore openings), making it difficult to justify the added complexity of a nonuniform site distribution.

Notation

List of Terms and Symbols

- A^{ig} Intragranular specific surface area obtained using the tracer method ($m^2\ g^{-1}$). (The superscript "*ig*" is used generally to denote an intragranular pore space quantity.)
- α_j Mass transfer coefficient for intragranular model domain j (h^{-1}).
- C Concentration (nCi mL^{-1} for tritium, nM for Br^-).
- C_i Initial concentration, typically taken to be the concentration just before the start of the washing stage in the WB experiment ($t < 0$).
- C_f Final concentration, typically taken to be the average concentration at $t > t_{eqlb}$.
- C^{eg} Aqueous concentration in the extragranular zone (nCi mL^{-1} or nM). (The superscript "*eg*" is used generally to denote an extragranular pore space quantity.)
- $C^{ig}_{t=0}$ Aqueous concentration in the intragranular zone at $t = 0$ (nCi mL^{-1} or nM). (Time $t = 0$, indicated with the subscript, is generally assigned as the start

of the tracer-release experiment at the moment the final clean-solution aliquot is added.)

D Diffusion coefficient

DB "Dry-batch" experiments, in which the pre-equilibration solution was removed by freeze-drying (tritium experiments only).

ε Intragranular pore volume as a fraction of sediment skeletal volume ($\varepsilon = \rho V^{ig}$) (dimensionless).

f^{eg} Extragranular fraction of the total tritium-hydrogen exchange sites (dimensionless).

f^{ig} Intragranular fraction of the total tritium-hydrogen exchange sites ($f^{ig} = 1 - f^{eg}$).

K_E Hydrogen/tritium exchange coefficient (mL g^{-1}).

m Sediment mass (g).

μ Mean of the lognormal distribution used to define mass transfer coefficients in the distributed-rate mass transfer model (log[h^{-1}]).

p/p^0 N_2 gas pressure divided by the saturation pressure at a given temperature (dimensionless).

q_{rel} Total quantity of tracer released in an experiment (mol).

$q_{aq,f}$ Final ($t > t_{eqlb}$) quantity of tracer present in solution (mol).

q_{samp} Total quantity of tracer sampled throughout the course of an experiment (mol).

$q^{eg}_{aq,f}$ Quantity of tracer present in the extragranular aqueous phase at $t > t_{eqlb}$ (mol).

Δq^{ig}_{aq} Change in the quantity of tracer in the intragranular aqueous phase (mol).

Δq^{ig}_{surf} Change tn the quantity of adsorbed tracer in the intragranular zone (mol).

Q_{surf} Adsorbed tracer concentration on a sediment mass basis (mol g^{-1}).

r Radial coordinate variable (mm).

R Radial coordinate variable normalized by sphere radius (dimensionless).

R^{ig} Intragranular retardation coefficient (dimensionless).

ρ Sediment skeletal density (g cm^{-3}).

ρ_b Sediment suspension bulk density (g cm^{-3}).

S Tritium-hydrogen exchange surface-site density (mol g^{-1} or sites nm^{-2}).

σ Standard deviation of the lognormal distribution used to define mass transfer coefficients in the distributed-rate mass transfer model (log[h^{-1}]).

t Time (h).

t_{eqlb} Time past which tracer release has reached equilibrium (h).

θ^{eg} Extragranular porosity (dimensionless).

θ^{ig}_j Porosity of intragranular model domain j (dimensionless).

v_j Solution volume (mL).

v^{ig} Intragranular pore volume (mL).

V^{ig} Intragranular specific pore volume (mm^3 g^{-1}).

WB "Wet-batch" experiments, in which the pre-equilibration solution was replaced with clean solution by repeated centrifugation, decanting, and backfilling.

x Fraction of exchange sites occupied by tritium (dimensionless).

[67] **Acknowledgments.** We thank Li Yang for assistance in N_2 gas adsorption analyses, as well as Douglas Kent, John Nimmo, William Ball, and two anonymous reviewers for helpful comments on the manuscript. This research was supported by the USGS Hydrologic Research and Development Program and by the U.S. Department of Energy, Office of Biological and Environmental Research (BER) Subsurface Biogeochemistry Research (SBR) Program through the Hanford Science Focus Area (SFA) and the Hanford Integrated Field Research Challenge (IFRC).

References

Appelo, C. A. J., and P. Wersin (2007), Multicomponent diffusion modeling in clay systems with application to the diffusion of tritium, iodide, and sodium in opalinus clay, *Environ. Sci. Technol.*, *41*(14), 5002–5007.

Arai, Y., M. A. Marcus, N. Tamura, J. A. Davis, and J. M. Zachara (2007), Spectroscopic evidence for uranium bearing precipitates in vadose zone sediments at the Hanford 300-Area site, *Environ. Sci. Technol.*, *41*, 4633–4639.

Ball, W. P., and P. V. Roberts (1991), Long-term sorption of halogenated organic chemicals by aquifer material. 2. Intraparticle diffusion, *Environ. Sci. Technol.*, *25*, 1237–1249.

Ball, W. P., C. H. Buehler, T. C. Harmon, D. M. Mackay, and P. V. Roberts (1990), Characterization of a sandy aquifer material at the grain scale, *J. Contam. Hydrol.*, *5*(3), 253–295.

Ball, W. P., M. N. Goltz, and P. V. Roberts (1991), Comment on "Modeling the transport of solutes influenced by multiprocess nonequilibrium" by M. L. Brusseau, R. E. Jessup, and P. S. C. Rao, *Water Resour. Res.*, *27*(4), 653–656, doi:10.1029/91WR00279.

Barrett, E. P., L. G. Joyner, and P. P. Halenda (1951), The determination of pore volume and area distributions in porous substances. I. Computations from nitrogen isotherms, *J. Am. Chem. Soc.*, *73*, 373–380.

Bond, D. L., J. A. Davis, and J. M. Zachara (2008), Uranium(VI) release from contaminated vadose zone sediments: Estimation of potential contributions from dissolution and desorption, in *Adsorption of Metals to Geomedia II*, edited by M. O. Barnett and D. B. Kent, p. 42, Elsevier, New York.

Brusseau, M. L., and P. S. C. Rao (1990), Modeling solute transport in structured soils: A review, *Geoderma*, *46*, 169–192.

Catalano, J., J. P. McKinley, J. M. Zachara, S. M. Heald, S. C. Smith, and G. E. Brown (2006), Changes in uranium speciation through a depth sequence of contaminated Hanford sediments, *Environ. Sci. Technol.*, *40*(8), 2517–2524.

Crank, J. (1975), *The Mathematics of Diffusion*, 2nd ed., 424 pp., Oxford Univ. Press, Oxford, U. K.

Culver, T. B., S. P. Hallisey, D. Sahoo, J. J. Deitsch, and J. A. Smith (1997), Modeling the desorption of organic contaminants from long-term contaminated soil using distributed mass transfer rates, *Environ. Sci. Technol.*, *31*(6), 1581–1588.

Cunningham, J. A., C. J. Werth, M. Reinhard, and P. V. Roberts (1997), Effects of grain-scale mass transfer on the transport of volatile organics through sediments. 1. Model development, *Water Resour. Res.*, *33*(12), 2713–2726, doi:10.1029/97WR02425.

Davis, J. A., and D. B. Kent (1990), Surface complexation modeling in aqueous geochemistry, in *Reviews in Mineralogy: Mineral Water Interface Geochemistry*, edited by M. F. Hochella and A. F. White, pp. 176–260, Mineralogical Society of America, Washington, D.C.

Deitsch, J. J., J. A. Smith, T. B. Culver, R. A. Brown, and S. A. Riddle (2000), Distributed-rate model analysis of 1,2-dichlorobenzene batch sorption and desorption rates for five natural sorbents, *Environ. Sci. Technol.*, *34*, 1469–1476.

Demir, I. (1988), Studies of smectite membrane behavior: Electrokinetic, osmotic, and isotopic fractionation processes at elevated pressures, *Geochim. Cosmochim. Acta*, *52*, 727–737.

Dennison, D. I., D. R. Sherwood, and J. S. Young (1989), *Status Rep. on Remedial Investigation of the 300 Area Process Ponds, PNL-6442*, 86 pp., Pacific Northwest National Laboratory, Richland, WA.

Ewing, R. P., Q. Hu, and C. Liu (2010), Scale dependence of intragranular porosity, tortuosity, and diffusivity, *Water Resour. Res.*, *46*, W06513, doi:10.1029/2009WR008183.

García-Gutiérrez, M., T. Missana, M. Mingarro, J. Samper, Z. Dai, and J. Molinero (2001), Solute transport properties of compacted Ca-bentonite used in FEBEX project, *J. Contam. Hydrol.*, *47*, 127–137.

Gregg, S. J., and K. S. W. Sing (1982), *Adsorption, Surface Area, and Porosity*, 2nd ed., 98 pp., Academic, New York.

Greskowiak, J., M. B. Hay, H. Prommer, C. Liu, V.E.A. Post, R. Ma, J. A. Davis, C. Zheng, and J. M. Zachara (2011), Simulating adsorption of U(VI) under transient groundwater flow and hydrochemistry: Physical

vs. chemical non-equilibrium model, *Water Resour. Res.*, *47*, W08501, doi:10.1029/2010WR010118.

Haggerty, R., and S. M. Gorelick (1995), Multiple-rate mass transfer for modeling diffusion and surface reactions in media with pore-scale heterogeneity, *Water Resour. Res.*, *31*(10), 2383–2400, doi:10.1029/95WR01583.

Horváth, G., and K. Kawazoe (1983), Method for the calculation of effective pore size distribution in molecular sieve carbon, *J. Chem. Eng. Jpn.*, *16*, 470–475.

Kleineidam, S., C. Schüth, and P. Grathwohl (2002), Solubility-normalized combined adsorption-partitioning sorption isotherms for organic pollutants, *Environ. Sci. Technol.*, *36*, 4689–4697.

Koch, S., and H. Flühler (1993), Non-reactive solute transport with micropore diffusion in aggregated porous media determined by a flow-interruption method, *J. Contam. Hydrol.*, *14*, 39–54.

Koretsky, C. M., D. A. Sverjensky, and N. Sahai (1998), A model of surface site types on oxide and silicate minerals based on crystal chemistry: Implications for site types and densities, multi-site adsorption, surface infrared spectroscopy, and dissolution kinetics, *Am. J. Sci.*, *298*, 349–438.

Leofanti, G., M. Padovan, G. Tozzola, and B. Venturelli (1998), Surface area and pore texture of catalysts, *Catal. Today*, *41*, 207–219.

Lippens, B. C., and J. H. de Boer (1965), Studies on pore systems in catalysts: V. The *t* method, *J. Catal.*, *4*(3), 319–323.

Liu, C. (2007), An ion diffusion model in semi-permeable clay materials, *Environ. Sci. Technol.*, *41*, 5403–5409.

Liu, C., J. M. Zachara, W. Yantasee, P. D. Majors, and J. P. McKinley (2006), Microscopic reactive diffusion of uranium in the contaminated sediments at Hanford, United States, *Water Resour. Res.*, *42*, W12420, doi:10.1029/2006WR005031.

Liu, C., J. M. Zachara, N. P. Qafoku, and Z. Wang (2008), Scale-dependent desorption of uranium from contaminated subsurface sediments, *Water Resour. Res.*, W08413, doi:10.1029/2007WR006478.

Liu, C., Z. Shi, and J. M. Zachara (2009), Kinetics of uranium(VI) desorption from contaminated sediments: Effect of geochemical conditions and model evaluation, *Environ. Sci. Technol.*, *43*, 6560–6566.

Ma, R., C. Zheng, H. Prommer, J. Greskowiak, C. Liu, J. M. Zachara, and M. Rockhold (2010), A field-scale reactive transport model for U(VI) migration influenced by coupled multirate mass transfer and surface complexation reactions, *Water Resour. Res.*, *46*, W05509, doi:10.1029/2009WR008168.

Mills, R. (1973), Self-diffusion in normal and heavy water in the range 1–45 deg., *J. Phys. Chem.*, *77*(5), 685–688.

Mooney, R. W., A. G. Keenan, and L. A. Wood (1952), Adsorption of water vapor by montmorillonite. I. Heat of desorption and application of BET theory, *J. Am. Chem. Soc.*, *74*(6), 1367–1371.

Nelson, N. T., Q. Hu, and M. L. Brusseau (2003), Characterizing the contribution of diffusive mass transfer to solute transport in sedimentary aquifer systems at laboratory and field scales, *J. Hydrol.*, *276*, 275–286.

Nkedi-Kizza, P., P. S. C. Rao, R. E. Jessup, and J. M. Davidson (1982), Ion exchange and diffusive mass transfer during miscible displacement through an aggregated oxisol, *Soil Sci. Soc. Am. J.*, *46*, 471–476.

Parker, J. C., and A. J. Valocchi (1986), Constraints on the validity of equilibrium and first-order kinetic transport models in structured soils, *Water Resour. Res.*, *22*(3), 399–407, doi:10.1029/WR022i003p00399.

Pedit, J. A., and C. T. Miller (1994), Heterogeneous sorption processes in subsurface systems. 1. Model formulations and applications, *Environ. Sci. Technol.*, *28*, 2094–2104.

Poeter, E. P., M. C. Hill, E. R. Banta, S. Mehl, and S. Christensen (2005), *UCODE_2005 and Six Other Computer Codes for Universal Sensitivity Analysis, Calibration, and Uncertainty Evaluation; U.S. Geological Survey Techniques and Methods 6-A11*, 283 pp., USGS, Reston, VA.

Qafoku, N. P., J. M. Zachara, C. Liu, P. L. Gassman, N. P. Qafoku, and S. C. Smith (2005), Kinetic desorption and sorption of U(VI) during reactive transport in a contaminated Hanford sediment, *Environ. Sci. Technol.*, *39*, 3157–3165.

Rao, P. S. C., D. E. Rolston, R. E. Jessup, and J. M. Davidson (1980a), Solute transport in aggregated porous media: Theoretical and experimental evaluation, *Soil Sci. Soc. Am. J.*, *44*, 1139–1146.

Rao, P. S. C., R. E. Jessup, D. E. Rolston, J. M. Davidson, and D. P. Kilcrease (1980b), Experimental and mathematical description of nonadsorbed solute transfer by diffusion in spherical aggregates, *Soil Sci. Soc. Am. J.*, *44*, 684–688.

Rügner, H., S. Kleineidam, and P. Grathwohl (1999), Long term sorption kinetics of phenanthrene in aquifer materials, *Environ. Sci. Technol.*, *33*, 1645–1651.

Saito, A., and H. C. Foley (1991), Curvature and parametric sensitivity in models for adsorption in micropores, *AIChE J.*, *37*, 429–436.

Serne, R. J., C. F. Brown, H. T. Schaef, E. M. Pierce, M. J. Lindberg, Z. Wang, P. L. Gassman, and J. Catalano (2002), *300 Area Uranium Leach and Adsorption Project, PNNL-14022*, 416 pp., Pacific Northwest National Laboratory, Richland, WA.

Sing, K. S. W. (1989), The use of gas adsorption for the characterization of porous solids, *Colloids Surf.*, *38*, 113–124.

Singer, D. M., J. M. Zachara, and G. E. Brown (2009), Uranium speciation as a function of depth in contaminated Hanford sediments—A micro-XRF, micro-XRD, and micro- and bulk-XAFS study, *Environ. Sci. Technol.*, *43*, 630–636.

Smit, W., C. L. M. Holten, H. N. Stein, J. J. M. De Goeij, and H. M. J. Theelen (1978), A radiotracer determination of the sorption of sodium ions by microporous silica films, *J. Colloid Interface Sci.*, *67*(3), 397–407.

Smit, W., C. L. M. Holten, and H. N. Stein (1981), Tritium exchange experiments on thin microporous silica layers, *J. Non-Cryst. Solids*, *43*, 279–295.

Stubbs, J. E., L. A. Veblen, D. C. Elbert, J. M. Zachara, J. A. Davis, and D. R. Veblen (2009), Newly recognized hosts for uranium in the Hanford Site vadose zone, *Geochim. Cosmochim. Acta*, *73*, 1563–1576.

van Genuchten, M. T., and P. J. Wierenga (1977), Mass transfer studies in sorbing porous media: II. Experimental evaluation with tritium ($3H_2O$), *Soil Sci. Soc. Am. J.*, *41*(2), 272–278.

Van Loon, L. R., and A. Jakob (2005), Evidence for a second transport porosity for the diffusion of tritiated water (HTO) in a sedimentary rock (opalinus clay—OPA): Application of through- and out-diffusion techniques, *Transp. Porous Media*, *61*, 193–214.

Van Loon, L. R., W. Müller, and K. Iijima (2005), Activation energies of the self-diffusion of HTO, $^{22}Na^{+}$, and ^{36}Cl in a highly compacted argillaceous rock (opalinus clay), *Appl. Geochem.*, *20*, 961–972.

Vidal, O., and B. Dubacq (2009), Thermodynamic modeling of clay dehydration, stability and compositional evolution with temperature, pressure and H_2O activity, *Geochim. Cosmochim. Acta*, *73*, 6544–6564.

Wang, K., and S.-J. Jiang (2008), Determination of iodine and bromine compounds by ion chromatography/dynamic reaction cell inductively coupled plasma mass spectrometry, *Anal. Sci.*, *24*, 509–514.

Werth, C. J., and M. Reinhard (1999), Counter-diffusion of isotopically labeled trichloroethylene in silica gel and geosorbent micropores: Column results, *Environ. Sci. Technol.*, *33*, 730–736.

Wood, W. W., T. F. Kraemer, and P. P. Hearn Jr. (1990), Intragranular diffusion: An important mechanism influencing solute transport in clastic aquifers?, *Science*, *247*, 1569–1572.

Yates, D. E. (1975), The structure of the oxide/aqueous electrolyte interface, Ph.D. thesis, 246 pp., Univ. Melbourne, Australia.

Yates, D. E., and T. W. Healy (1976), The structure of the silica/electrolyte interface, *J. Colloid Interf. Sci.*, *55*, 9–19.

Yates, D. E., R. O. James, and T. W. Healy (1980), Titanium dioxide-electrolyte interface. Part 1. Gas adsorption and tritium exchange studies, *J. Chem. Soc., Faraday Trans. 1*, *76*, 1–8.

Zachara, J. M., J. A. Davis, C. Liu, J. P. McKinley, N. P. Qafoku, D. M. Wellman, and S. B. Yabusaki (2005), *Uranium Geochemistry in Vadose Zone and Aquifer Sediments from the 300 Area Uranium Plume, PNNL-15121*, 113 pp., Pacific Northwest National Laboratory, Richland, WA.

Zhang, S., D. B. Kent, D. C. Elbert, Z. Shi, J. A. Davis, and D. R. Veblen (2011), Mineralogy, morphology, and textural relationships in coatings on quartz grains in sediments in a quartz-sand aquifer, *J. Contam. Hydrol.*, *124*, 57–67.

J. A. Davis, Lawrence Berkeley National Lab, 1 Cyclotron Road Mail Stop 90-1116, Berkeley, CA, 94720, USA.

M. B. Hay and D. L. Stoliker, Water Resources Division, U.S. Geological Survey, 345 Middlefield Rd., Mail Stop 496, Menlo Park, CA 94025, USA. (mbhay@usgs.gov)

J. M. Zachara, Pacific Northwest National Laboratory, PO Box 999, Richland, Washington 99352, USA.